Retrieval techniques for airborne imaging of methane concentrations using high spatial and moderate spectral resolution: Application to AVIRIS

A. K. Thorpe[1], C. Frankenberg[2], and D. A. Roberts[1]

[1]{Department of Geography, University of California, Santa Barbara, Santa Barbara, California, USA}

[2]{Jet Propulsion Laboratory, California Institute of Technology, Pasadena, California, USA}

Correspondence to: A. K. Thorpe (akthorpe@geog.ucsb.edu)

Abstract

Two quantitative retrieval techniques were evaluated to estimate methane (CH_4) enhancement in concentrated plumes using high spatial and moderate spectral resolution data from the Airborne Visible/Infrared Imaging Spectrometer (AVIRIS). An Iterative Maximum a Posteriori Differential Optical Absorption Spectroscopy (IMAP-DOAS) algorithm performed well for an ocean scene containing natural CH_4 emissions from the Coal Oil Point (COP) seep field near Santa Barbara, California. IMAP-DOAS retrieval precision errors are expected to equal between 0.31 to 0.61 ppm CH_4 over the lowest atmospheric layer (height up to 1.04 km), corresponding to about a 30 to 60 ppm error for a 10 m thick plume. However, IMAP-DOAS results for a terrestrial scene were adversely influenced by the underlying landcover. A hybrid approach using Singular Value Decomposition (SVD) was particularly effective for terrestrial surfaces because it could better account for spectral variability in surface reflectance. Using this approach, a CH_4 plume was observed extending 0.1 km ~~immediately~~ downwind of two hydrocarbon storage tanks at the Inglewood Oil Field in Los Angeles, California, with a maximum near surface enhancement of 8.45 ppm above background. At COP, the distinct plume had a maximum enhancement of 2.85 ppm CH_4 above background, ~~and was consistent with known seep locations and local wind direction~~ and extended more than 1 km downwind of known seep locations. A sensitivity analysis also indicates CH_4

sensitivity should be more than doubled for the next generation AVIRIS sensor (AVIRISng) due to improved spectral resolution and sampling. AVIRIS-like sensors offer the potential to better constrain emissions on local and regional scales, including sources of increasing concern like industrial point source emissions and fugitive CH_4 from the oil and gas industry.

Keywords: Iterative Maximum a Posteriori Differential Optical Absorption Spectroscopy (IMAP-DOAS), Singular Value Decomposition (SVD), Retrieval, Methane, CH_4, Concentration, Fugitive, Emissions, Point source, Plume, Coal Oil Point (COP) seep field, Inglewood Oil Field, Los Angeles, Airborne Visible/Infrared Imaging Spectrometer, AVIRIS

1 Introduction

Atmospheric methane (CH_4) is a long-lived greenhouse gas with an instantaneous radiative forcing 21 times greater than carbon dioxide (CO_2) on a per molecule basis (IPCC, 2007). In the late preindustrial Holocene (1000 to 1800 A.D.), mean concentrations were 695 ppb (Etheridge et al., 1998) and global concentrations have increased to around 1800 ppb in 2013 (NOAA, 2013). While anthropogenic sources made up an estimated 4 to 34% of pre-industrial emissions (IPCC, 2007; Houweling et al., 2000), between 60 and 70% of emissions are presently anthropogenic (Lelieveld et al., 1998). Further, ice core records have indicated CH_4 concentrations are closely tied to atmospheric temperature records, while present-day concentrations have not been observed in the previous 420,000 years (Wuebbles and Hayhoe, 2002).

While the global CH_4 budget is relatively well constrained (550 +/- 50 Tg CH_4 yr^{-1}), there is considerable uncertainty regarding partitioning between individual natural and anthropogenic source types and locations (IPCC, 2007). Major sources of anthropogenic CH_4 emissions include the energy, industrial, agricultural, and waste management sectors. In the United States, 50% of anthropogenic CH_4 emissions are from the energy sector, including natural gas and oil systems, coal mining, and stationary/mobile combustion (EPA, 2011). Global fugitive CH_4 emissions from natural gas and oil systems are of increasing concern, estimated at 1,354.42 million metric tons~~MMT~~ CO_2 E yr^{-1} (64.50 Tg CH_4 yr^{-1}) and expected to increase 35% by 2020 (EPA, 2006). Recent studies also suggest official inventories are underestimated, for example, top-down estimates indicate fugitive CH_4 emissions are between

2.3 and 7% of CH_4 produced annually for the Denver-Julesburg Basin, Colorado (Petron et al., 2012). In the Los Angeles Basin, CH_4 emissions appear underestimated (Wunch et al., 2009) and unaccounted sources appear to be fugitive and natural CH_4 emissions (Wennberg et al., 2012).

Significant natural CH_4 sources include wetlands, termites, and geological seeps (IPCC, 2007). Globally, geological seeps are highly uncertain but estimated to contribute between 20 to 40 Tg CH_4 yr^{-1} for terrestrial environments (Etiope et al., 2009) and about 40 Tg CH_4 yr^{-1} for marine seepage (Kvenvolden and Rogers, 2005). In addition, increased surface and ocean temperatures associated with global warming may increase CH_4 emissions from melting permafrost (Woodwell et al., 1998) and CH_4 hydrate destabilization (Kvenvolden, 1988).

2 Airborne measurements of CH_4

Aircraft measurements of gas concentrations are useful because they offer the potential to measure local/regional variations in gas concentrations and complement ongoing efforts at coarser spatial resolutions, such as spaceborne sensors. These airborne measurements can improve greenhouse gas emissions inventories and offer the potential for detection and monitoring of emissions (NRC, 2010).

Research and commercial aircraft equipped with in situ gas measurement provides some sense of CH_4 variability at local and regional scales (ARCTAS, 2010; Schuck et al., 2012). The nadir-viewing Fourier Transform Spectrometer (FTS) included as part of the Carbon in Arctic Reservoirs Vulnerability Experiment (CARVE) (Miller and Dinardo, 2012) and spectrometers like MAMAP (Methane Airborne MAPper) (Gerilowski et al., 2011) also offer the potential to measure local emissions. For example, MAMAP detected elevated CH_4 concentrations from coal mine ventilation shafts near Ibbenbüren, Germany ~~(Krings et al., 2013)~~allowing for an inversion estimate that agreed closely with emission rates reported from mine operators (Krings et al., 2013). However, these non-imaging spectrometers have a small field of view (FOV) and are limited to flying transects across local gas plumes rather than mapping plumes in their entirety.

By combining large image footprints and fine spatial resolution, airborne imaging spectrometers are well suited for mapping local CH_4 plumes. ~~However, increased spatial resolution requires reduced spectral resolution, thereby decreasing detection sensitivity.~~ The

Airborne Visible/Infrared Imaging Spectrometer (AVIRIS) has a 34° FOV and measures reflected solar radiance at the nadir viewing geometry across 224 channels between 350 and 2,500 nm (Green et al., 1998). Strong CH_4 absorption features present between 2,000 and 2,500 nm can be observed at a 10 nm spectral resolution ~~sampling~~ and Full Width Half Maximum (FWHM). These absorptions are clearly shown in Fig. 1 by transmittance spectra calculated for CH_4 using Modtran 5.3 (Berk et al., 1989), parameterized for a mid-latitude summer model atmosphere and nadir-looking sensor at 8.9 km altitude. High resolution transmittance is shown in red for Fig. 1a and convolved to AVIRIS wavelengths in Fig. 1b, while water vapour (H_2O) transmittance has been included in blue to indicate spectral overlap with CH_4.

These shortwave infrared (SWIR) absorptions have permitted mapping of concentrated gas plumes in both marine and terrestrial environments using AVIRIS. For bright sun-glint scenes at the Coal Oil Point (COP) marine seep field in the Santa Barbara Channel, California, Roberts et al. (2010) developed a spectral residual approach between 2,000 and 2,500 nm and Bradley et al. (2011) a band ratio technique using the 2,298 nm CH_4 absorption band and 2,058 nm carbon dioxide (CO_2) absorption band. However, these techniques are not suited for terrestrial locations that have lower albedos and have spectral structure in the SWIR. A Cluster-Tuned Matched Filter (CTMF) technique is capable of mapping CH_4 plumes from marine and terrestrial sources (Thorpe et al., 2013) as well as CO_2 from power plants (Dennison et al., 2013), however, this method does not directly quantify gas concentrations.

The logical next step is to focus on quantification and uncertainty estimation using techniques originally developed for satellite sensors such as Differential Optical Absorption Spectroscopy (DOAS) (Platt, 1994). In this study, an Iterative Maximum a Posteriori Differential Optical Absorption Spectroscopy (IMAP-DOAS) (Frankenberg et al., 2005c) algorithm was adapted for gas detection in AVIRIS imagery. In addition, a hybrid approach using Singular Value Decomposition (SVD) and IMAP-DOAS was also developed as a complementary method of quantifying gas concentrations within complex AVIRIS scenes.

3 Basic principles of IMAP-DOAS

Retrieval algorithms for absorbing species in the SWIR require radiative transfer modelling of solar radiation along the light path to the sensor and must be capable of simulating changes in radiation due to differing abundances of absorbers. These techniques permit comparison of simulated at sensor radiance with a known abundance of absorbers with measured radiance provided by the sensor. Differential Optical Absorption Spectroscopy (DOAS) (Platt, 1994) is one approach that has been used for a number of applications, including ground-based (Stutz et al., 2010), satellite (Schneising et al., 2012), and airborne measurement (Gerilowski et al., 2011). The underlying principle of DOAS is to isolate higher frequency features resulting from gas absorptions from lower frequency features that include surface reflectance as well as Rayleigh and Mie scattering (Bovensmann et al., 2011). To do so, a polynomial function accounting for low-frequency features is often used, which is described in further detail in Section 5.2.

Classical DOAS (Platt, 1994) is based on the Lambert-Beer law and describes the relationship between incident intensity for the vertical column ($I_0(v)$) and measured intensity ($I(v)$) after passing through a light path (ds) containing ~~multiple~~ an absorber~~s~~:

$$I(v) = I_0(v) \cdot \exp(-\int \sigma(v, p, T) c(s) ds). \quad (1)$$

Each absorber has an associated absorption cross section (σ) and number concentration of the absorber ($c(s)$, molecules/m^3). Equation (1) is wavelength dependent and the absorption cross section varies with temperature (T) and pressure (p). If the atmospheric absorption features are fully resolved by the instument and only weak absorbers are present~~For ideal instruments (or weak absorbers),~~, Eq. (1) can be linearized with respect to slant column density S:

$$\vec{\tau} = \ln\left(\frac{I_0(v)}{I(v)}\right) \approx \sigma(v, \bar{p}, \bar{T}) \cdot \int c(s) ds = \sigma(v, p, T) \cdot S. \quad (2)$$

where measured ~~differential~~ optical density ($\vec{\tau}$) is proportional to the product of the absorption cross section and the retrieved S, the path integral of the concentration of the absorber along the lightpath. S is related to the vertical column density (V), the integral of the concentration along the vertical from the surface to the top of atmosphere, by way of the airmass factor (A), where $A=S/V$. In the SWIR, scattering in the atmosphere is generally low (Buchwitz and Burrows, 2003; Dufour and Breon, 2003) and for our applications, the impact of scattering is far lower than the retrieval precision error. Thus, it can be neglected and A=1/cos(SZA)+1/cos(LZA), where SZA is the solar zenith angle and LZA is the line of sight zenith angle. However, scattering could become non-negligible in some examples, including industrial plumes that contain heavy aerosol loading or dark surfaces with low SZA.

For a single absorber measured with a moderate spectral resolution and ignoring scattering, a theoretical slant optical density ($\vec{\tau}_\lambda^{meas}$) can be calculated as follows

$$\vec{\tau}_{\lambda}^{meas}(x) = -\ln(< \exp(-x \cdot A \cdot \vec{\tau}_{\lambda}^{ref}) >). \quad (3)$$

where the reference vertical optical density ($\vec{\tau}_{\lambda}^{ref}$) is scaled by both the airmass factor (A) as well as a retrieved scaling factor (x) and <·> denotes convolution with the instrument function. In addition to scaling $\vec{\tau}_{\lambda}^{meas}$, x can be used to estimate gas concentrations relative to those concentrations present within the reference atmosphere.

However, moderate spectral resolution spectrometers cannot fully resolve individual absorption lines and must convolve light using an instrument lineshape (ILS) function wider than individual absorption lines. If absorptions are strong, ~~T~~this results in a non-linear relationship between the measured ~~differential~~ optical density ($\vec{\tau}$) and the retrieved slant column density of the absorber (S) shown in Eq. (2) (Frankenberg et al., 2005c). ~~Further, optical densities can be large in the SWIR, especially i~~In the 2,300 nm region, ~~with its~~ strong H_2O and CH_4 absorption lines are saturated within their line cores ~~strengths~~. These factors render ~~invalidate~~ Eq. (2) non-linear and cause classical DOAS algorithms to fail, requiring iterative procedures to account for the induced non-linearity ~~for moderate spectral resolution spectrometers and strong absorbers~~.

To address the strong sensitivity of the shape of spectral absorption lines to temperature and pressure as well as unresolved absorption lines (Platt and Stutz, 2008), the Weighting Function Modified Differential Optical Absorption Spectroscopy (WFM-DOAS) retrieval algorithm was developed (Buchwitz et al., 2000). WFM-DOAS introduced weighting functions to linearize the problem about a linearization point in the expected slant column density using vertical profiles of all absorbers as well as pressure and temperature profiles. It has been used to estimate column amounts of CO (carbon monoxide), CO_2, and CH_4 using Scanning Imaging Absorption Spectrometer for Atmospheric Chartography (SCIAMACHY) data, which has a spectral ~~sampling interval~~resolution between 0.2 and 1.5 nm (Buchwitz et al., 2005). A modified WFM-DOAS algorithm is used with the airborne MAMAP, which has a SWIR grating spectrometer for measuring CH_4 and CO_2 absorptions between 1,590 and 1,690 nm with a 0.82 nm FWHM (Gerilowski et al., 2011)~~(Krings et al., 2011)~~. In addition to detecting elevated CH_4 concentrations from coal mines (Krings et al., 2013), MAMAP has been used to measure both CH_4 and CO_2 emissions from power plants ~~(Gerilowski et al., 2011)~~ (Krings et al., 2011).

Frankenberg et al. (2005c) developed the IMAP-DOAS algorithm, which uses optimal estimation theory to adjust the slant column densities of multiple gasses until total optical density fits the observed measurement. IMAP-DOAS considers the shape of the spectral absorption lines as they vary with temperature and pressure in multiple atmospheric layers and convolves absorption lines using the instrument lineshape function. This technique is based on a simple non-scattering radiative transfer scheme, which allows very fast retrievals and is well suited for processing of AVIRIS imagery. For the 2,300 nm range, where Rayleigh scattering can be ignored and aerosol optical depths are low, this assumption in IMAP-DOAS is valid given errors induced by neglected scattering in AVIRIS scene are typically much lower (0 to 2%) than precision errors in retrieved column estimates (>3%). Additional details of the IMAP-DOAS algorithm and retrieval method are presented in Sect. 5.

While IMAP-DOAS has been used with SCIAMACHY data to estimate global column-averaged mixing ratios for CH_4 (Frankenberg et al., 2005a; Frankenberg et al., 2011) and CO (Frankenberg et al., 2005b), this study is the first to use aircraft measurements. Moderate resolution spectrometers like AVIRIS require large fitting windows and disentangling surface spectral features from atmospheric absorptions becomes more complicated using fitting routines such as WFM-DOAS and IMAP-DOAS. High resolution spectrometers can circumvent this problem since atmospheric absorption lines are narrow and surface properties, which vary on a scale greater than 5 to 10 nm, can be fitted using polynomial functions. In this case, reflectance spectra of terrestrial surfaces (not including narrow atmospheric features) can ususally be represented by a low order polynmial as a function of wavelength. For the 10 nm spectral resolution ~~sampling~~ and FWHM of AVIRIS, distinguishing surface features from atmospheric absorptions will be more difficult. Therefore, we developed an alternative hybrid approach using both IMAP-DOAS and SVD of surface reflectance properties at background CH_4 concentrations.

4 Study sites and AVIRIS data

Two AVIRIS scenes were used in this study, both acquired in California in 2008. The first scene was acquired over the COP marine seep field near Santa Barbara from an 8.9 km altitude, resulting in an image swath of ~5.4 km and a ground instantaneous field of view (IFOV) of ~7.5 m. The scene was acquired on 19 June 2008 at approximately 19:55 UTC

(12:55 PDT)~~-~~ with a 11.4° solar zenith resulting in high sun-glint. COP is one of the largest natural seeps with total atmospheric CH_4 emissions estimated at 100,000 $m^3 day^{-1}$ (0.024 Tg CH_4 yr^{-1}) (Hornafius et al., 1999). A 308 by 191 pixel image subset was used for the IMAP-DOAS and SVD algorithms, covering 3.31 km^2 centered on the COP seep field (34°23'46.59"N, 119°52'4.47"W).

The second scene covered the Inglewood Oil Field, located in Los Angeles in an area that has active oil and gas extraction (DOGGR, 2010). The AVIRIS scene was acquired at approximately 21~~0~~:12 UTC (14:12 PDT) on 18 September 2008 at 4.0 km altitude, resulting in a swath width of ~2.7 km, ground IFOV of ~3 m, and a 38.1° solar zenith. For this scene, a 161 by 172 pixel image subset (0.25 km^2 centered at 33°59'28.68"N, 118°21'34.59"W) was selected because it contains a CH_4 plume detected using a CTMF technique, with hydrocarbon storage tanks as a probable emission source (Thorpe et al., 2013).

5 IMAP-DOAS retrieval method

The IMAP-DOAS retrieval relies on layer optical properties of absorbing species calculated for a realistic temperature/pressure and trace gas concentration profile for a given location. In addition, instrument lineshape and flight parameters are used with geometric radiative transfer calculations to simulate at-sensor radiances and Jacobians with respect to trace gas abundances for each atmospheric layer. In the following, we describe input parameters and additional details of the IMAP-DOAS retrieval.

5.1 IMAP-DOAS input parameters

For the two 2008 AVIRIS scenes, temperature, pressure, and H_2O volume mixing ratio (VMR) profiles acquired from the National Centers for Environmental Prediction/National Center for Atmospheric Research (NCEP/NCAR) Reanalysis project were extracted for the appropriate date and time for either location (Kalnay et al., 1996). The NCEP data are provided on a 2.5° latitude × 2.5° longitude grid every 6 hours with 17 pressure levels between 10 and 1,000 mb. Prior profiles of CH_4 and N_2O are based on the U.S. standard atmosphere obtained from the radiative transfer models LOWTRAN/MODTRAN (Kneizys et al., 1996). These profiles were scaled to reflect the VMR for CH_4 and N_2O using the 2008 mean VMR provided from the NOAA Mauna Loa station, United States (NOAA, 2013). For both gasses, the percent increase of the 2008 mean VMR compared to the U.S. standard atmosphere at 0 km altitude was calculated and used to update the VMR up to 25 km altitude. Finally, we computed vertical optical depths for 10 atmospheric layers at 100 mb intervals between 0 and 1,000 mb.

For AVIRIS, the strongest CH_4 absorptions occur between 2,200 to 2,400 nm (Fig. 1). Spectral parameters for CH_4, H_2O, and N_2O were used from the HITRAN database (Rothman et al., 2009). We used a classical Voigt spectral line-shape to calculate CH_4, H_2O, and N_2O vertical optical densities for each of the 10 atmospheric layers.

Given that the two AVIRIS scenes were acquired at different flight altitudes and SZA, geometric air mass factors (AMF) had to be calculated for each of the 10 layers to account for either one (above sensor) or two (below sensor) way transmission through each layer. For example, the COP flight was at 8.9 km altitude with a solar zenith angle of 11.4°, placing the aircraft approximately at the boundary between atmospheric layer 3 and 4 (Fig. 2). In this simplified setup, the AMF for layers 1 to 3 (above the aircraft) is calculated as 1/cos(11.4°)=1.02, while for layers 4 to 10, an AMF of 2.02 (1/cos(11.4°)+1/cos(0.0°)) accounts for two way transmission. Similar calculations were performed for the Los Angeles scene, which was acquired with a SZA of 38.1° at 4.0 km altitude placing the aircraft approximately at the boundary between layer 5 and 6.

Additional input parameters for the IMAP-DOAS algorithm are shown in Fig. 3, including the AVIRIS radiance data, spectral resolution ~~sampling~~ of the sensor, signal-to-noise ratio (SNR) estimate, and the full width at half maximum of the instrument line-shape (FWHM=10.42 nm, assuming a Gaussian line-shape). An average FWHM and SNR was calculated for bands included within the fitting window, while the high resolution solar transmission spectrum was generated using a solar linelist (Geoffrey Toon, personal communication, 2013).

The optimal choice of a fitting window for the IMAP-DOAS CH_4 retrievals was determined iteratively. We began using all spectral bands between 2,100 and 2,500 nm corresponding to strong CH_4 absorptions, but observed strong correlations with surface features. This is likely related to spectrally smooth convolved transmissions from 2,200 to 2,300 nm and above 2,370 nm (Fig. 1b). As we decreased the size of the fitting window to focus on the more high-frequency CH_4 features, the spectral variability associated with AVIRIS bands at either end of the fitting window was reduced and results improved. The fitting window selected for this study used 9 bands between 2,278 and 2,358 nm, including three prominent absorption features visible in CH_4 Jacobians shown in Fig. 4a.

5.2 Forward model and optimal estimation

Using 10 atmospheric layers and the gasses CH_4, H_2O, and N_2O results in a state vector with 30 rows ($\vec{x}_n$). ~~In principle, N_2O could be neglected at this spectral resolution but we included it for the sake of completeness.~~ A forward radiative transfer model at high spectral resolution was used to calculate modeled radiance at each wavelength using the equation below

$$\vec{F}^{hr}(\vec{x}_i) = \vec{I}_0^{hr} * \exp\left(-\sum_{n=1}^{30} \vec{A}_n \cdot \vec{\tau}_n^{ref} \cdot \vec{x}_{n,i}\right) * \sum_{i=0}^{k} a_k \lambda^k. \quad (4)$$

where

$\vec{F}^{hr}(\vec{x}_i)$ is the forward modeled radiance at the i-th iteration of the state vector,

$\vec{I}_0^{hr}$ is the incident intensity (solar transmission spectrum),

$\vec{A}_n$ is the AMF for each n ~~layer of each gas~~ number of atmospheric state vector elements (30 rows, specified for each of the 10 layers and repeated for each gas),

$\vec{\tau}_n^{ref}$ is the reference total optical density for each n number of atmospheric state vector elements ~~layer~~ (~~the sum of~~including optical densities of CH_4, H_2O, and N_2O),

$\vec{x}_{n,i}$ is the trace gas related state vector at the i-th iteration, which scales the prior optical densities of CH_4, H_2O, and N_2O in each n layer (30 rows).

a_k are polynomial coefficients to account for low-frequency spectral variations.

The high resolution modeled radiance is then convolved with the ILS and sampled to the center wavelengths of each AVIRIS spectral band. This results in a low resolution modeled radiance at the i-th iteration of the state vector ($\vec{F}^{lr}(\vec{x}_i)$), calculated using a known $\vec{\tau}_n^{ref}$ scaled by $\vec{x}_{n,i}$.

In addition to the ~~priors~~ scaling factors for CH_4, H_2O, and N_2O in each n layers ($\vec{x}_n$), the state vector ~~($\vec{x}_a$)~~ contains the spectral shift (not shown here) as well as a low order polynomial function (a_k) to account for the broad-band variability in surface albedo (see Frankenberg et al., 2005c).

At each iteration i, a Jacobian Matrix is calculated where each column represents the derivate vector of the sensor radiance with respect to each element of the state vector ($\vec{x}_i$).

$$\mathbf{K}_i = \left.\frac{\partial \vec{\mathbf{F}}^{lr}(\vec{x})}{\partial \vec{x}}\right|_{\vec{x}_i}. \quad (5)$$

The forward model and the Jacobian Matrix can be used to optimize the state vector at the i-th iteration as follows (Rodgers, 2000)

$$\vec{x}_{i+1} = \vec{x}_a + (\mathbf{K}_i^T \mathbf{S}_\varepsilon^{-1} \mathbf{K}_i + \mathbf{S}_a^{-1})^{-1}\, \mathbf{K}_i^T \mathbf{S}_\varepsilon^{-1} \cdot \left[\vec{y} - \vec{F}^{lr}(\vec{x}_i) + \mathbf{K}_i(\vec{x}_i - \vec{x}_a)\right]. \quad (6)$$

where

$\vec{x}_a$ is the a priori state vector (30 rows),

$\vec{x}_i$ is the state vector at the i-th iteration (30 rows),

$\mathbf{S}_\varepsilon$ is the error covariance matrix,

$\mathbf{S}_a$ is the a priori covariance matrix,

$\vec{y}$ is the measured AVIRIS radiance,

$\vec{F}^{lr}(\vec{x}_i)$ is the forward model evaluated at $\vec{x}_i$,

$\mathbf{K}_i$ is the Jacobian of the forward model at $\vec{x}_i$.

The a priori state vector was set to 1 for each gas at each layer, while the a priori covariance matrix was set to constrain the fit to the lowest atmospheric layer (height up to 1.04 km) where high variance is expected. To achieve this, very tight prior covariances were set for all atmospheric layers except the lowermost one, which is basically unconstrained. This assumption is reasonable given that the COP and Inglewood scenes contain CH_4 emission from ground sources that are not expected to extend above this atmospheric layer. CH_4 concentrations were calculated by multiplying the CH_4 state vector at the last iteration (CH_4 scaling factor) by the VMR for the lowest layer of the reference atmosphere (Fig. 2).

6 Basic principles of SVD

SVD transforms a large number of potentially correlated vectors into a smaller set of uncorrelated (orthogonal) vectors, denoted as singular vectors (Press et al., 2007; Rodgers, 2000). It is closely related to Principal Component Analysis (PCA) and offers the potential for reduced computation time by efficiently summarizing high dimensional data. It has been used in a number of remote sensing applications, including cloud detection using the Michelson Interferometer for Passive Atmospheric Sounding (MIPAS) (Hurley et al., 2009), retrieving aerosol optical densities of mineral dust using the Infrared Atmospheric Sounding Interferometer (IASI), and retrieval of terrestrial chlorophyll fluorescence using the Fourier

Transform Spectrometer (FTS) onboard the Greenhouse gases Observing SATellite (GOSAT) platform (Guanter et al., 2012).

For this study, we constructed an m × n matrix **L**, where m is the number of spectral bands (for the CH_4 fit window) and n is the number of radiance spectra in a specific AVIRIS scene. This can be expressed as

$$\mathbf{L} = \mathbf{U}\mathbf{\Lambda}\mathbf{V}^{\mathrm{T}}. \quad (7)$$

where the m × m matrix **U** contains the left singular vectors and the n × n matrix **V** contains the right singular vectors in their respective columns. **Λ** is an m × n rectangular diagonal matrix containing the m singular values of **L** on its diagonal. These singular values are essentially eigenvalues that correspond to the m columns of **U**, which are analogous to eigenvectors. Each of the n columns of **V** is essentially a principal component of the scene, with each successive column capturing increasingly less signal variability. Therefore, **L** can be recomposed as a linear combination of singular vectors scaled by the singular values (Murtagh and Heck, 1987).

7 SVD retrieval method

For each AVIRIS image subset, the radiance scene was first standardized by fitting a first order polynomial to each radiance spectrum and dividing it by the polynomial fit. Next, a mean radiance spectrum was calculated from the standardized data and the IMAP-DOAS retrieval was performed on the mean spectrum to generate the CH_4 Jacobian for the lowest layer ($\mathbf{K}_{CH4}$) (Fig. 5). This standardization was performed to ensure that the computed CH_4 Jacobian is representative for all pixels; without it, calculations of Jacobians for each continuum level would be required. As an alternative to standardization, a SVD in log-space could be considered since optical depths are linear with respect to changing concentrations in the vicinity of the linearization point.

Using Eq. 7, the SVD was performed on each image subset using the standardized radiance (m × n matrix **L**, where m is the number of spectral bands and n is the number of radiance spectra). Due to computing limitations, the economy version of the SVD was calculated using MATLAB (Mathworks, Natick, Massachusetts). This resulted in $\mathbf{U}_{econ}$ maintaining a dimension of m × m (left singular vectors in m columns), but reduced matrix dimensions for $\mathbf{V}_{econ}$ and $\mathbf{\Lambda}_{econ}$ (n × m and m × m respectively).

The first c columns of $\mathbf{U}_{econ}$ ($\mathbf{U}_{select}$, an m × c matrix where the optimal selection of c is described below) and the CH_4 Jacobian ($\mathbf{K}_{CH4}$, an m × 1 matrix) are concatenated to generate a matrix **J** (dimensions of m × c+1). The basic principle is to reflect the general variability in spectral radiances by a linear combination of the first c eigenvectors and the CH_4 Jacobian, which relates to deviations from background concentrations since the background radiance is already modeled using the linear combination of eigenvectors. A similar technique was used to retrieve terrestrial chlorophyll fluorescence using the FTS onboard GOSAT (Guanter et al., 2012). The linear combination of eigenvectors is an empirical way to compute the forward model radiance, which can include many detector and surface albedo features that the IMAP-DOAS approach cannot easily handle.

Using linear least squares, we can now find a vector $\boldsymbol{W}$ that minimizes the cost function involving the measured radiance spectra $\boldsymbol{y}$:

$$||\boldsymbol{y} - \mathbf{J}\boldsymbol{W}||^2. \quad (8)$$

$\boldsymbol{W}$ represents the contribution of each column of **J** to the measured radiance. The modeled radiance $\boldsymbol{F}$ can be calculated by multiplying **J** by the weights $\boldsymbol{W}$:

$$\boldsymbol{F} = \mathbf{J}\boldsymbol{W}. \quad (9)$$

resulting in a modeled radiance that can be compared to the measured radiance for each spectrum.

The previous equation can be rewritten as the sum of the background and CH_4 component of the radiance as follows:

$$\boldsymbol{F}(\boldsymbol{W},\mathbf{J}) = \sum_{k=1}^{c} \mathbf{J}_k \cdot \boldsymbol{W}_k + \mathbf{J}_{c+1} \cdot \boldsymbol{W}_{c+1} \quad (10)$$

where the left term represents the background radiance modeled as a linear combination of the first c eigenvectors of **J** ($\mathbf{J}_k$) multiplied by the corresponding weights $\boldsymbol{W}_k$. The right term is the CH_4 component of the scene, the product of $\mathbf{J}_{c+1}$ (the CH_4 Jacobian, $\mathbf{K}_{CH4}$) and its corresponding weight $\boldsymbol{W}_{c+1}$ (denoted as RCH_4). In Equation (10), the fit coefficients are c and $\boldsymbol{W}$. RCH_4 indicates how much of the observed radiance for each spectrum can be associated with the CH_4 Jacobian (i.e. changes in absorptions due to CH_4) and can be used to both estimate CH_4 concentrations as well as its uncertainties. Similar to the IMAP-DOAS approach, RCH_4 for each pixel is multiplied by the VMR for the lowest layer of the reference atmosphere and results in an estimated CH_4 concentration in ppm above/below the average.

The same 9 bands between 2,278 and 2,358 nm that made up the IMAP-DOAS retrieval window were initially used for the hybrid SVD approach. In an iterative process, additional bands between 2,218 and 2,457 nm were included to better account for high frequency variation present in the scenes. A portion of the scene was selected for a homogeneous landcover and the standard deviation of the RCH_4 results for different fitting windows was calculated. A 16 band fitting window (2,278 to 2,428 nm) was selected because it produced the lowest standard deviation in RCH_4 and thereby minimized noise in results.

Using these 16 bands, the hybrid SVD retrieval was performed iteratively by increasing the c columns of $\mathbf{U}_{econ}$ used to generate $\mathbf{U}_{select}$. This resulted in 16 SVD retrievals, which were assessed by minimizing the standard deviation of the RCH_4 results for the portion of the scene selected to represent homogeneous landcover. This technique was used to determine the optimal number of columns of $\mathbf{U}_{econ}$ to use with the SVD retrieval for the COP and Inglewood scenes.

8 Results for IMAP-DOAS sensitivity study

To investigate the expected IMAP-DOAS retrieval errors for the 9 band fitting window between 2,278 and 2,358 nm, the covariance $\hat{\mathbf{S}}$ was calculated using the following equation

$$\hat{\mathbf{S}} = (\mathbf{K}^T \mathbf{S}_\varepsilon^{-1} \mathbf{K} + \mathbf{S}_a^{-1})^{-1}. \quad (11)$$

where the diagonal of $\hat{\mathbf{S}}$ corresponds to the covariance associated with CH_4, H_2O, and N_2O at each of the 10 atmospheric layers. $\mathbf{S}_\varepsilon$ is the error covariance matrix, a diagonal matrix representing expected errors resulting from shot-noise and dark current that is calculated using the SNR for the AVIRIS sensor.

The precision error of the IMAP-DOAS retrieval algorithm is calculated by multiplying the square root of the corresponding diagonal entry of $\hat{\mathbf{S}}$ (the standard deviation of the CH_4 fit factor) by 1.78 ppm CH_4, the 2008 mean VMR provided from the NOAA Mauna Loa station, United States (NOAA, 2013). These errors were calculated for a number of hypothetical sensors with varying spectral~~-~~ resolution~~sampling intervals (SSI)~~ and FWHM across a range of SNR (Fig. 6). As expected, the IMAP-DOAS error decreases as SNR increases and as the spectral resolution ~~sensor SSI~~ and FWHM become finer. The black line (10 nm spectral resolution~~SSI~~ and FWHM) approximates the AVIRIS sensor and the SNR for bands used in the IMAP-DOAS retrieval was conservatively estimated between 100 and 200 using an

AVIRIS instrument model for low albedo surfaces (Rob Green, personal communication, 2013). Using scene parameters similar to the COP flight (8.9 km altitude, 11.4° solar zenith), this corresponds to an error of between 0.31 to 0.61 ppm CH_4 over the lowest atmospheric layer (up to 1.04 km) shown in Fig. 2a. Given that about 10% of the total column is within the lowest layer, this error is considerable and roughly corresponds to an error of 30 to 60 ppb in column-averaged CH_4 over the total atmospheric column.

9 Results for IMAP-DOAS

9.1 COP

For the COP subset shown in Fig. 7a, measured radiance for the first band of the IMAP-DOAS retrieval window at 2,278 nm had a maximum of 6.436 (sensor saturation), minimum of 0.1158, maximum of 6.436 (sensor saturation), and mean of 2.0516 microwatt·cm^{-2}·sr^{-1}·nm^{-1} (uWcm^{-2}sr^{-1}nm^{-1}.). Sensor saturation occurs only for a small portion of the scene where the full well of the detector is saturated for multiple channels in the SWIR. Sonar return contours of subsurface CH_4 bubble plumes are overlain and correspond to known seep locations (Leifer et al., 2010). In Figure 7b, the CH_4 scaling factor is shown for the lowest atmospheric layer (height up to 1.04 km) and a CH_4 enhancement is clearly visible consistent with emission from seep locations and the 2.3 ms^{-1} southwesterly wind measured at the nearby West Campus Station. The standard deviation of the residual (the difference between measured and modeled radiance) was also calcuated to evaluate the ability of IMAP-DOAS to model radiance. This result is shown in Fig. 7c and has a similar visual appearance to Fig. 7a, indicating a strong albedo influence.

CH_4 concentrations were calculated by multiplying the retrieved CH_4 scaling factor by the VMR for the lowest atmospheric layer (1.78 ppm CH_4). In Figure 7d, ppm CH_4 for the lowest layer is shown (subcolumn XCH_4), excluding 740 bright pixels (greater than 5 uWcm^{-2}sr^{-1}nm^{-1} in the fitting window) associated with high standard deviation of the residuals. These results indicate enhancements in the lowest layer up to 2.5 times concentrations present in the reference atmosphere, equivalent to 4.46 ppm CH_4 averaged across the distance from the ocean surface to 1.04 km. However, there appears to be a positive bias in these results given concentrations for locations upwind of the plume appear higher than the expected background concentration of 1.78 ppm. Therefore, the subcolumn XCH_4 results appear overestimated. This observed bias will be further addressed in Sect. 11.

In Figure 7, location L1 and L2 correspond to the measured and modeled radiance plotted in Fig. 8. At location L1 (Fig. 8a), the measured radiance (black) is nearly horizontal for wavelengths between 2,278 and 2,328 nm, indicating sensor saturation due to high sun-glint. This causes considerable disagreement with the modeled radiance (red) as indicated by the residual radiance shown in the bottom plot; this pixel was excluded from the results shown in Fig. 7d. For Figure 8b (location L2), the radiance is considerably lower and there is better agreement between measured and modeled radiance, resulting in a retrieved concentration of 2.18 ppm CH_4 for this pixel. This radiance was detrended in Fig. 8c and the CH_4 Jacobian for the lowest layer is overlain to indicate the location of CH_4 absorptions at 2,298, 2,318, and 2,348 nm.

9.2 Inglewood

The Inglewood subset (Fig. 9a) is highly heterogeneous, with a maximum measured radiance of 0.8033, minimum of 0.0192, and mean of 0.2800 $uWcm^{-2}sr^{-1}nm^{-1}$ at 2,278 nm. A road crosses the scene from north to south, separating the Inglewood Oil Field on the left from a residential neighborhood on the right. In this complex urban environment, the low order polynomial in the IMAP-DOAS algorithm is unable to account for some of the high frequency spectral variability that interferes with CH_4 absorptions. Therefore, the CH_4 scaling factor results for the lowest atmospheric layer are heavily influenced by the land surface type (Fig. 9b). For example, the road appears clearly visible and high CH_4 scaling factors occur for individual structures within the neighborhood. Dark spectra also appear to have erroneously high CH_4 scaling factors, including heavily vegetated areas in the northwest and southeast of the scene.

For the lowest atmospheric layer, subcolumn XCH_4 results are shown in Fig. 9d, excluding dark pixels less than 0.1 $uWcm^{-2}sr^{-1}nm^{-1}$ in the fitting window. While background concentrations are expected around 1.78 ppm CH_4, observed background concentrations appear biased upward, between 2 and 3 ppm. Despite the noisy results, a feature of elevated CH_4 is visible in the center of the image with maximum concentrations in excess of 5.5 ppm. This CH_4 plume is consistent with a 2.2 ms^{-1} southwesterly wind measured nearby at the time of image acquisition (weatherunderground.com, 2012). Using higher resolution Google Earth imagery acquired one year after the AVIRIS flight, two hydrocarbon storage tanks were identified immediately upwind and are the probable emission source (Fig. 9e).

10 Results for SVD

10.1 COP

While the IMAP-DOAS technique permitted CH_4 retrievals for the more homogeneous marine location, high frequency variation present in the terrestrial example interferes with CH_4 absorptions and makes mapping more challenging. To permit retrievals for terrestrial locations, a hybrid approach using SVD and IMAP-DOAS was used to first account for high frequency variation present in the scene and determine what variance of the standardized radiance resulted from changes in CH_4.

In Figure 10, all 16 columns of $\mathbf{U}_{econ}$ are shown in addition to the CH_4 Jacobian ($\mathbf{K}_{CH4}$). Following the iterative method described in Sect. 7, 4 of the total 16 columns of $\mathbf{U}_{econ}$ were used to generate $\mathbf{U}_{select}$ and account for over 99.99% of the variance. Next, $\mathbf{U}_{select}$ and $\mathbf{K}_{CH4}$ were concatenated to generate the **J** matrix, which is used for modelling radiance (see Eq. 9).

In Figure 11b the weights (RCH_4) associated with the column of **J** that corresponds to the CH_4 Jacobian are shown (see Eq. 9). Within the scene, expected background values are 0 and the distinctive CH_4 plume is similar to the IMAP-DOAS results (Fig. 7b). In Figure 12d, ppm CH_4 relative to background is shown excluding 323 pixels (0.55% of total scene) associated with standard deviation of the residuals greater than 0.0075 (Fig. 11c; a unitless value given the SVD was performed on standardized radiance). CH_4 concentrations exceed 3 ppm above background within the plume, gradually decrease downwind, and approach expected background concentrations.

10.2 Inglewood

Using the iterative method described in Sect. 7, 9 columns of $\mathbf{U}_{econ}$ were selected to generate $\mathbf{U}_{select}$ for the Inglewood scene. The RCH_4 results (Fig. 12b) more clearly distinguish the CH_4 plume compared to the IMAP-DOAS results (Fig. 9b), however, the SVD standard deviation of the residuals indicates higher errors for vegetated surfaces (Fig. 12c). Excluding pixels with greater than 0.0075 standard deviation of the residual, retrieved concentrations relative to background are shown in Fig. 12d. Expected background concentrations are observed throughout much of the scene and CH_4 concentrations are highest for the western portion of the plume (in excess of 4 ppm above background).

In Figure 12, location L3 and L4 correspond to the measured and modeled radiance plotted in Fig. 13. At location L3 (Fig. 13a), there is considerable disagreement between the measured (black) and modeled radiance (red) as indicated by the residual. L3 is located in a vegetated region and because the standard deviation of the residual exceeds 0.0075, this pixel was excluded from the results shown in Fig. 12d. In contrast, there is good agreement for L4, which is made up of bare soil with an estimated concentration of 0.38 ppm CH_4 above background (Fig. 13b).

As described in Section 9.2, high standard deviation of the residuals were observed for dark pixels in IMAP-DOAS results for the Inglewood scene (Fig. 9c). In Fig. 9d, dark pixels less than 0.1 $uWcm^{-2}sr^{-1}nm^{-1}$ in the fitting window were excluded from IMAP-DOAS results, which included vegetated surfaces. For the hybrid approach using SVD and IMAP-DOAS, pixels with greater than 0.0075 standard deviation of the residual were excluded from the results shown in Fig. 12d, also corresponding to vegetation within the scene. The average radiance at 2,278 nm for those pixels with greater than 0.0075 standard deviation of the residual for the hybrid approach (Fig. 12d, black pixels) was only 0.1368 $uWcm^{-2}sr^{-1}nm^{-1}$ compared to the 0.3129 $uWcm^{-2}sr^{-1}nm^{-1}$ average for the remaining pixels in the scene. Dark pixels and their corresponding low SNR cause lower single measure precision and are thus problematic for both the IMAP-DOAS and the hybrid approach.

11 Discussion

11.1 Comparison of retrieval results

The IMAP-DOAS and hybrid SVD approach were capable of quantifying CH_4 concentrations from plumes over marine and terrestrial environments. For both techniques, agreement between measured and modeled radiance was poorest at albedo extremes, for example saturated pixels at COP and dark, vegetated surfaces at Inglewood. SVD results indicate near surface enhancements relative to background; absorptions resulting from background CH_4 concentrations in the scene are contained in $\mathbf{U}_{select}$ and the retrieval used the CH_4 Jacobian from the lowest layer of the atmospheric model. Similarly, the IMAP-DOAS retrieval also provides ppm CH_4 enhancements averaged over the lowest atmospheric layer (up to 1.04 km).

For the IMAP-DOAS results from COP and Inglewood, an average background ppm CH_4 concentration was calculated for the portion of the scene selected to represent homogeneous landcover (see Sect. 7). To account for the observed positive bias in subcolumn XCH_4 (see Sect. 9), this average concentration was subtracted from subcolumn XCH_4, resulting in ppm CH_4 relative to background. However, different portions of each scene were excluded from IMAP-DOAS and SVD results due to observed biases. For example, pixels were excluded from IMAP-DOAS results at Inglewood using an albedo threshold (Fig. 9d), while a standard deviation of the residual threshold was applied to SVD results (Fig. 12d). To permit comparison between results, only those pixels not excluded from either the IMAP-DOAS or SVD results are shown in Fig. 14 and Fig. 15.

These results were also ~~validated against~~compared with an independent technique, the Cluster-Tuned Matched Filter (CTMF) that was applied to both scenes (Fig. 14c and Fig. 15c). ~~The CTMF uses a gas transmittance spectrum as a target to calculate CTMF scores for each image pixel where scores greater than one indicate significant evidence of the gas signature (Thorpe et al., 2013; Funk et al., 2001).~~ The CTMF is trained with a gas transmittance spectrum as a target to calculate CTMF scores for each image pixel where scores greater than one indicate significant evidence of the gas signature (Funk et al., 2001). Because the CTMF uses the inverse of the scene's covariance structure to remove large-scale noise to isolate the gas signal, it is best suited for detecting concentrated sources rather than background concentrations. A detailed description of the CTMF algorithm including results from both the COP and Inglewood image subsets is available in Thorpe et al., 2013. The CTMF does not provide an estimate of gas concentrations, rather it provides an image of gas anomalies that can be evaluated for consistency with probable emissions sources and local wind direction. In contrast, IMAP-DOAS and the hybrid SVD approach provide CH_4 concentrations as well as uncertainty estimates.

At COP, there is good spatial agreement between the observed plumes obtained with the IMAP-DOAS (Fig. 14a), hybrid SVD (Fig. 14b), and CTMF (Fig. 14c) approaches (Thorpe et al., 2013). IMAP-DOAS CH_4 concentrations are generally higher (mean 0.12, standard deviation 0.43 ppm relative to background) than the SVD results (mean -0.01, standard deviation 0.63 ppm relative to background). The location of an identical transect is shown for the IMAP-DOAS (Fig. 14a, green line), SVD (Fig. 14b, cyan), and CTMF results (Fig. 14c, red). At each point along the transect, an average value was calculated for 21 pixels centered on the transect in the horizontal direction. The average values along the transect are plotted in Fig. 14d and indicate concentrations for IMAP-DOAS (green) are generally higher than for the SVD approach (cyan) with both transects sharing the cyan figure axes. Where the transect intersects the plume, there is good agreement in the pronounced peak in values from the three techniques, including CTMF results (red) that were offset for clarity and correspond to the red figure axes. While the CTMF technique appears better suited for detecting diffuse portions of the plume (Fig. 14c), it does not provide CH_4 concentrations.

Using the hybrid SVD approach, the maximum observed concentration within the scene was 2.85 ppm CH_4 above background, located at a region of subsurface CH_4 bubble plumes as shown by the sonar return contours (Fig. 11a). Averaged over the lowest atmospheric layer (a distance of 1.04 km), this maximum concentration will increase when scaled for a smaller atmospheric column. For example, concentrations increase to 590 ppm CH_4 above background if all enhancements are within a 5 m atmospheric column. Near surface concentrations are likely much higher; Leifer et al. (2006) measured up to 2×10^4 ppm CH_4 at 5 m height using a flame ion detector.

For Inglewood, the CH_4 plume is clearly visible in IMAP-DOAS (Fig. 15a), hybrid SVD (Fig. 15b), and CTMF (Fig. 15c) results (Thorpe et al., 2013). CH_4 concentrations for IMAP-DOAS are generally higher (mean 0.13 and standard deviation 1.03 ppm relative to background) than the hybrid SVD results (mean -0.04 and standard deviation 1.60 ppm relative to background). Overall there is good spatial agreement for the observed CH_4 plume obtained using these three distinct techniques.

Similar to the COP comparison, the location of an identical transect is shown for the IMAP-DOAS, SVD, and CTMF results. An average was calculated at each point along the transect (for 9 pixels centered on the transect in the vertical direction) and plotted in Fig. 15d, indicating two locations with enhanced CH_4 between the 70th and 100th pixels. For this portion of the transect, there is considerable disagreement between the IMAP-DOAS (Fig. 15d, green line) and SVD concentrations (blue). This discrepancy can be partly attributed to the influence of the choice of the number of columns of $\mathbf{U}_{econ}$ used to generate $\mathbf{U}_{select}$ (see Section 7). For the transect shown in Fig. 15d, 9 columns of $\mathbf{U}_{econ}$ were used, resulting in a mean concentration along the transect of 0.4141 ppm CH_4 relative to background. Selecting 10 columns of $\mathbf{U}_{econ}$

decreased the mean concentration along the transect to 0.3664 ppm relative to background with a standard deviation of the difference between transects obtained using 9 and 10 columns equal to 0.2959 ppm. In contrast, using 8 columns of $\mathbf{U}_{econ}$ results in a mean concentration of 0.4144 ppm relative to background and the standard deviation of the difference between transects obtained using 9 and 8 columns is reduced to 0.1508 ppm relative to background. This indicates that retrieved CH_4 concentrations obtained using the SVD approach is influenced by the choice of $\mathbf{U}_{select}$ because higher-order singular vectors can start correlating with the computed CH_4 Jacobian.

For the SVD approach at Inglewood using 9 columns of $\mathbf{U}_{econ}$, the maximum within the CH_4 plume was 8.45 ppm above background with concentrations decreasing downwind of the hydrocarbon storage tanks (Fig. 12d). Such enhancements are feasible given tanks represent large emission sources; natural gas storage tanks can emit between 4.3 and 42.0 × 10^{-4} Gg CH_4 per (10^6) m^3 gas withdrawals per year (IPCC, 2000) and tank venting represented approximately 14.4% (212 Gg CH_4) of the total U.S. CH_4 emissions from petroleum systems in 2009 (EPA, 2011).

11.2 Potential for AVIRISng and future sensors

While CH_4 retrievals are promising using AVIRIS, the next generation sensor (AVIRISng) will have a 5 nm spectral resolution~~SSI~~ and FWHM that should significantly improve CH_4 sensitivity. An IMAP-DOAS retrieval error between 0.31 to 0.61 ppm CH_4 over the lowest atmospheric layer (height up to 1.04 km) is expected for an AVIRIS scene acquired at 8.9 km altitude, 11.4° solar zenith, and with a SNR conservatively set between 100 and 200 (Fig. 6, black line). This corresponds to about a 32 to 63 ppm retrieval error for a 10 m thick plume or 322 to 634 ppm for a 1 m thick plume. For a similar AVIRISng scene, the IMAP-DOAS retrieval error would be reduced to between 0.18 to 0.35 ppm over the lowest atmospheric layer for the same range of SNR (Fig. 6, red line), however retrieval errors remain significant. In addition, SNR for AVIRISng should be considerably improved, further reducing retrieval errors.

To further assess this increased sensitivity, CH_4 Jacobians were calculated for AVIRISng and AVIRIS for a 5% CH_4 enhancement over the lowest atmospheric layer. In Figure 16a, the AVIRIS CH_4 Jacobian (black line) has a -4.7 × 10^{-4} $\Delta uWcm^{-2}sr^{-1}nm^{-1}/\Delta VMR$ amplitude between a peak at 2,310 nm and the CH_4 absorption at 2,320 nm. For AVIRISng (red line) this amplitude is -9.8 × 10^{-4} $\Delta uWcm^{-2}sr^{-1}nm^{-1}/\Delta VMR$, roughly representing a doubling of CH_4 sensitivity compared with AVIRIS. However, additional improvements should result from a greater number of detector pixels and the improved SNR of AVIRISng. Sensors with a finer spectral resolution~~SSI~~ and FWHM offer the potential for even greater sensitivity, as shown by the grey line in Fig. 16a for a spectral resolution~~SSI~~ and FWHM of 1 nm and reduced IMAP-DOAS retrieval errors indicated by the grey dashed line in Fig. 6.

12 Conclusions

In this study, two retrieval techniques were used to measure CH_4 enhancements for concentrated plumes over marine and terrestrial locations in AVIRIS data. The IMAP-DOAS algorithm performed well for the homogenous ocean scene containing the COP seeps and retrieval errors are estimated between 0.31 to 0.61 ppm CH_4 over the lowest atmospheric layer (height up to 1.04 km). For the Inglewood subset, IMAP-DOAS results became heavily influenced by the underlying landcover, while the hybrid SVD approach was particularly effective given that it could better account for spectrally variable surface reflectance. Using the hybrid SVD approach for the COP and Inglewood plumes, maximum near surface concentrations were 2.85 and 8.45 ppm CH_4 above background respectively. An additional benefit of the hybrid SVD approach is that it requires less than half the computational time of the IMAP-DOAS retrieval.

Given a 5 nm spectral resolution~~SSI~~ and FWHM, CH_4 sensitivity should be more than doubled for AVIRISng. This might permit CH_4 retrievals for weaker absorption features centered at 1,650 nm, as well as CO_2 retrievals for absorptions at 1,572, 1,602, and 2,058 nm. However, both the AVIRIS and AVIRISng sensors were not designed for detecting gas plumes and sensitivity could be dramatically improved using a spectrometer designed exclusively for mapping gas plumes. For example, an imaging spectrometer with 0.05 nm spectral resolution~~SSI~~ and 0.15 nm FWHM would have an IMAP-DOAS error around 18 times smaller than AVIRIS.

While non-imaging spectrometers such as MAMAP have increased CH_4 sensitivity compared to AVIRIS and AVIRISng, they are currently limited to flying transects across local gas plumes due to a small field of view. In contrast, airborne imaging spectrometers combine large image footprints and fine spatial resolution necessary to map local CH_4 plumes in their entirety however have considerably higher expected errors for retrieved CH_4 concentrations. ~~.~~

In this study, the observed COP plume extended more than 1 km, however, the Inglewood plume was much smaller, extending only 0.1 km downwind. Such plumes with a small spatial extent are of increasing concern, including industrial point source emissions, leaking gas pipelines (Murdock et al., 2008), and fugitive CH_4 from the oil and gas industryemissions (Howarth et al., 2011). Imaging spectrometers permit direct attribution of emissions to individual point sources which is particularly useful given the large uncertainties associated with anthropogenic emissions, including fugitive CH_4 emissions from the oil and gas industry (Petron et al., 2012; EPA, 2013; Allen et al., 2013), and the projected increase in these types of emissions (EPA, 2006). Therefore, AVIRIS-like sensors offer the potential to better constrain emissions on local and regional scales (NRC, 2010), improve greenhouse gas budgets and partitioning between natural and anthropogenic sources, as well as complement data provided at coarser spatial resolutions.

Acknowledgements

NCEP Reanalysis data provided by the NOAA/OAR/ESRL PSD, Boulder, Colorado, USA, from their web site at http://www.esrl.noaa.gov/psd/. The authors would like to thank Debra Wunch for aiding in generating NCEP atmospheric profiles and for the continued support of Robert Green and the rest of the AVIRIS/AVIRISng team at the Jet Propulsion Laboratory. In addition, we thank Joseph McFadden for his insightful comments. This work was supported by NASA Headquarters under the NASA Earth and Space Science Fellowship Program grant NNX13AM95H.

References

Allen, D. T., Torres, V. M., Thomas, J., Sullivan, D. W., Harrison, M., Hendler, A., Herndon, S. C., Kolb, C. E., Fraser, A., Hill, D., Lamb, B. K., Miskimins, J., Sawyer, R. F., and Seinfeld, J. H.: Measurements of methane emissions at natural gas production sites in the United States, P Natl Acad Sci, 110, 2013.

ARCTAS: Arctic Research of the Composition of the Troposphere from Aircraft and Satellites (ARCTAS), National Aeronautics and Space Administration (NASA), 2010.

Berk, A., Bernstein, L. S., and Robertson, D. C.: MODTRAN: A moderate resolution model for LOWTRAN7, AFGL-TR-89-0122, MA: Hanscom Air Force Base, 1989.

Bovensmann, H., Doicu, A., Stammes, P., Van Roozendael, M., von Savigny, C., Penning de Vries, M., Beirle, S., Wagner, T., Chance, K., Buchwitz, M., Kokhanovsky, A., Richter, A., Rozanov, A. V., and Rozanov, V. V.: From Radiation Fields to Atmospheric Concentrations – Retrieval of Geophysical Parameters, in: SCIAMACHY – Exploring the Changing Earth's Atmopshere, edited by: Gottwald, M. and Bovensmann, H., Springer, Dordrecht, 2011.

Bradley, E. S., Leifer, I., Roberts, D. A., Dennison, P. E., and Washburn, L.: Detection of marine methane emissions with AVIRIS band ratios, Geophys Res Lett, 38, L10702, doi 10.1029/2011GL046729, 2011.

Buchwitz, M., Rozanov, V. V., and Burrows, J. P.: A near-infrared optimized DOAS method for the fast global retrieval of atmospheric CH_4, CO, CO_2, H_2O, and N_2O total column amounts from SCIAMACHY Envisat-1 nadir radiances, J Geophys Res-Atmos, 105, 15231-15245, 2000.

Buchwitz, M., de Beek, R., Noel, S., Burrows, J. P., Bovensmann, H., Bremer, H., Bergamaschi, P., Korner, S., and Heimann, M.: Carbon monoxide, methane and carbon dioxide columns retrieved from SCIAMACHY by WFM-DOAS: year 2003 initial data set, Atmos Chem Phys, 5, 3313-3329, 2005.

Dennison, P. E., Thorpe, A. K., Pardyjak, E.R., Roberts, D. A., Qi, Y., Green, R.O., Bradley, E. S., Funk, C. C.: High spatial resolution mapping of elevated atmospheric carbon dioxide using airborne imaging spectroscopy: radiative transfer modeling and power plant plume detection, Remote Sens Environ, 2013, in press.

DOGGR: Online Production and Injection Query, State of California Department of Conservation, Division of Oil, Gas & Geothermal Resources (DOGGR), http://opi.consrv.ca.gov/opi/opi.dll, 2010.

EPA: Global Anthropogenic Non-CO_2 Greenhouse Gas Emissions: 1990-2020, United States Environmental Protection Agency (EPA), Washington, D.C., 274, 2006.

EPA: Inventory of U.S. Greenhouse Gas Emissions and Sinks: 1990-2009, United States Environmental Protection Agency (EPA), Washington, D.C., 459, 2011.

EPA: Inventory of U.S. Greenhouse Gas Emissions and Sinks: 1990-2011, United States Environmental Protection Agency (EPA), Washington, D.C., 505, 2013.

Etheridge, D. M., Steele, L. P., Francey, R. J., and Langenfelds, R. L.: Atmospheric methane between 1000 AD and present: Evidence of anthropogenic emissions and climatic variability, J Geophys Res-Atmos, 103, 15979-15993, doi 10.1029/98jd00923, 1998.

Etiope, G., Feyzullayev, A., and Baciu, C. L.: Terrestrial methane seeps and mud volcanoes: A global perspective of gas origin, Mar Petrol Geol, 26, 333-344, doi 10.1016/j.marpetgeo.2008.03.001, 2009.

Frankenberg, C., Meirink, J. F., van Weele, M., Platt, U., and Wagner, T.: Assessing methane emissions from global space-borne observations, Science, 308, 1010-1014, doi 10.1126/science.1106644, 2005a.

Frankenberg, C., Platt, U., and Wagner, T.: Retrieval of CO from SCIAMACHY onboard ENVISAT: detection of strongly polluted areas and seasonal patterns in global CO abundances, Atmos Chem Phys, 5, 1639-1644, 2005b.

Frankenberg, C., Platt, U., and Wagner, T.: Iterative maximum a posteriori (IMAP)-DOAS for retrieval of strongly absorbing trace gases: Model studies for CH4 and CO2 retrieval from near infrared spectra of SCIAMACHY onboard ENVISAT, Atmos Chem Phys, 5, 9-22, 2005c.

Frankenberg, C., Aben, I., Bergamaschi, P., Dlugokencky, E. J., van Hees, R., Houweling, S., van der Meer, P., Snel, R., and Tol, P.: Global column-averaged methane mixing ratios from 2003 to 2009 as derived from SCIAMACHY: Trends and variability, J Geophys Res-Atmos, 116, D04302, doi 10.1029/2010jd014849, 2011.

Funk, C. C., Theiler, J., Roberts, D. A., and Borel, C. C.: Clustering to improve matched filter detection of weak gas plumes in hyperspectral thermal imagery, Ieee T Geosci Remote, 39, 1410-1420, 2001.

Gerilowski, K., Tretner, A., Krings, T., Buchwitz, M., Bertagnolio, P. P., Belemezov, F., Erzinger, J., Burrows, J. P., and Bovensmann, H.: MAMAP - a new spectrometer system for column-averaged methane and carbon dioxide observations from aircraft: instrument description and performance analysis, Atmos Meas Tech, 4, 215-243, doi 10.5194/amt-4-215-2011, 2011.

Green, R. O., Eastwood, M. L., Sarture, C. M., Chrien, T. G., Aronsson, M., Chippendale, B. J., Faust, J. A., Pavri, B. E., Chovit, C. J., Solis, M. S., Olah, M. R., and Williams, O.:

Imaging spectroscopy and the Airborne Visible Infrared Imaging Spectrometer (AVIRIS), Remote Sens Environ, 65, 227-248, 1998.

Guanter, L., Frankenberg, C., Dudhia, A., Lewis, P. E., Gomez-Dans, J., Kuze, A., Suto, H., and Grainger, R. G.: Retrieval and global assessment of terrestrial chlorophyll fluorescence from GOSAT space measurements, Remote Sens Environ, 121, 236-251, doi 10.1016/j.rse.2012.02.006, 2012.

Hornafius, J. S., Quigley, D., and Luyendyk, B. P.: The world's most spectacular marine hydrocarbon seeps (Coal Oil Point, Santa Barbara Channel, California): Quantification of emissions, J Geophys Res-Oceans, 104, 20703-20711, 1999.

Houweling, S., Dentener, F., and Lelieveld, J.: Simulation of preindustrial atmospheric methane to constrain the global source strength of natural wetlands, J Geophys Res-Atmos, 105, 17243-17255, 2000.

Howarth, R. W., Santoro, R., and Ingraffea, A.: Methane and the greenhouse-gas footprint of natural gas from shale formations, Climatic Change, 106, 679-690, doi 10.1007/s10584-011-0061-5, 2011.

Hurley, J., Dudhia, A., and Grainger, R. G.: Cloud detection for MIPAS using singular vector decomposition, Atmos Meas Tech, 2, 533-547, 2009.

IPCC: Good Practice Guidance and Uncertainty Management in National Greenhouse Gas Inventories, Cambridge Univ. Press, New York, 2000.

IPCC: Climate Change 2007: The Physical Science Basis. Contribution of Working Group I to the Fourth Assessment Report of the Intergovernmental Panel on Climate Change, Intergovernmental Panel on Climate Change (IPCC), Cambridge Univ. Press, New York, 881, 2007.

Kalnay, E., Kanamitsu, M., Kistler, R., Collins, W., Deaven, D., Gandin, L., Iredell, M., Saha, S., White, G., Woollen, J., Zhu, Y., Chelliah, M., Ebisuzaki, W., Higgins, W., Janowiak, J., Mo, K. C., Ropelewski, C., Wang, J., Leetmaa, A., Reynolds, R., Jenne, R., and Joseph, D.: The NCEP/NCAR 40-year reanalysis project, B Am Meteorol Soc, 77, 437-471, Doi 10.1175/1520-0477(1996)077<0437:Tnyrp>2.0.Co;2, 1996.

Kneizys, F. X., Abreu, L. W., Anderson, G. P., Chetwynd, J. H., Shettle, E. P., Robertson, D. C., Acharya, P., Rothman, L., Selby, J. E. A., Gallery, W. O., and Clough, S. A.: The

MODTRAN 2/3 report and LOWTRAN 7 model, Tech. rep., Phillips Laboratory, Geophysics Directorate, Hanscom AFB, 1996.

Krings, T., Gerilowski, K., Buchwitz, M., Reuter, M., Tretner, A., Erzinger, J., Heinze, D., Pfluger, U., Burrows, J. P., and Bovensmann, H.: MAMAP - a new spectrometer system for column-averaged methane and carbon dioxide observations from aircraft: retrieval algorithm and first inversions for point source emission rates, Atmos Meas Tech, 4, 1735-1758, doi 10.5194/amt-4-1735-2011, 2011.

Krings, T., Gerilowski, K., Buchwitz, M., Hartmann, J., Sachs, T., Erzinger, J., Burrows, J. P., and Bovensmann, H.: Quantification of methane emission rates from coal mine ventilation shafts using airborne remote sensing data, Atmos Meas Tech, 6, 151-166, doi 10.5194/amt-6-151-2013, 2013.

Kvenvolden, K. A.: Methane Hydrate - a Major Reservoir of Carbon in the Shallow Geosphere, Chem Geol, 71, 41-51, 1988.

Kvenvolden, K. A., and Rogers, B. W.: Gaia's breath - global methane exhalations, Mar Petrol Geol, 22, 579-590, doi 10.1016/j.marpetgeo.2004.08.004, 2005.

Leifer, I., Luyendyk, B. P., Boles, J., and Clark, J. F.: Natural marine seepage blowout: Contribution to atmospheric methane, Global Biogeochem Cy, 20, Gb3008, doi 10.1029/2005gb002668, 2006.

Leifer, I., Kamerling, M. J., Luyendyk, B. P., and Wilson, D. S.: Geologic control of natural marine hydrocarbon seep emissions, Coal Oil Point seep field, California, Geo-Mar Lett, 30, 331-338, doi 10.1007/s00367-010-0188-9, 2010.

Lelieveld, J., Crutzen, P. J., and Dentener, F. J.: Changing concentration, lifetime and climate forcing of atmospheric methane, Tellus B, 50, 128-150, 1998.

Miller, C. E., and Dinardo, S. J.: CARVE: The Carbon in Arctic Reservoirs Vulnerability Experiment, Aerospace Conference, 2012 IEEE, 2012.

Murdock, D. G., Stearns, S. V., Lines, R. T., Lenz, D., Brown, D. M., and Philbrick, C. R.: Applications of real-world gas detection: Airborne Natural Gas Emission Lidar (ANGEL) system, J Appl Remote Sens, 2, 023518, 023518, doi 10.1117/1.2937078, 2008.

Murtagh, F., and Heck, A.: Multivariate Data Analysis, D. Reidel Publishing Company, Dordrecht, Holland, 1987.

NOAA: GMD Measurement Locations, National Oceanic & Atmospheric Administration (NOAA), Earth System Research Laboratory, Global Monitoring Division, 2013.

NRC: Verifying Greenhouse Gas Emissions: Methods to Support International Climate Agreements, Committee on Methods for Estimating Greenhouse Gas Emissions, National Research Council (NRC), The National Academies Press, Washington, D.C., 125 pp., 2010.

Petron, G., Frost, G., Miller, B. R., Hirsch, A. I., Montzka, S. A., Karion, A., Trainer, M., Sweeney, C., Andrews, A. E., Miller, L., Kofler, J., Bar-Ilan, A., Dlugokencky, E. J., Patrick, L., Moore, C. T., Ryerson, T. B., Siso, C., Kolodzey, W., Lang, P. M., Conway, T., Novelli, P., Masarie, K., Hall, B., Guenther, D., Kitzis, D., Miller, J., Welsh, D., Wolfe, D., Neff, W., and Tans, P.: Hydrocarbon emissions characterization in the Colorado Front Range: A pilot study, J Geophys Res-Atmos, 117, D04304, doi 10.1029/2011jd016360, 2012.

Platt, U.: Differential optical absorption spectroscopy (DOAS), in Air Monitoring by

Spectroscopic Techniques, John Wiley, New York, 1994.

Platt, U., and Stutz, J.: Differential optical absorption spectroscopy: principles and applications, Springer-Verlag, Berlin Heidelberg, 2008.

Press, W. H., Teukolosky, S. A., Vetterling, W. T., and Flannery, B. P.: Numerical recipes: The art of scientific computing, Vol. 3, Cambridge University Press, Cambridge, 2007.

Roberts, D. A., Bradley, E. S., Cheung, R., Leifer, I., Dennison, P. E., and Margolis, J. S.: Mapping methane emissions from a marine geological seep source using imaging spectrometry, Remote Sens Environ, 114, 592-606, doi 10.1016/j.rse.2009.10.015, 2010.

Rodgers, C. D.: Inverse Methods for Atmospheric Sounding, Theory and Practice, World Scientific, London, 2000.

Rothman, L. S., Gordon, I. E., Barbe, A., Benner, D. C., Bernath, P. E., Birk, M., Boudon, V., Brown, L. R., Campargue, A., Champion, J. P., Chance, K., Coudert, L. H., Dana, V., Devi, V. M., Fally, S., Flaud, J. M., Gamache, R. R., Goldman, A., Jacquemart, D., Kleiner, I., Lacome, N., Lafferty, W. J., Mandin, J. Y., Massie, S. T., Mikhailenko, S. N., Miller, C. E., Moazzen-Ahmadi, N., Naumenko, O. V., Nikitin, A. V., Orphal, J., Perevalov, V. I., Perrin, A., Predoi-Cross, A., Rinsland, C. P., Rotger, M., Simeckova, M., Smith, M. A. H., Sung, K., Tashkun, S. A., Tennyson, J., Toth, R. A., Vandaele, A. C., and Vander Auwera, J.: The

HITRAN 2008 molecular spectroscopic database, J Quant Spectrosc Ra, 110, 533-572, doi 10.1016/j.jqsrt.2009.02.013, 2009.

Schneising, O., Bergamaschi, P., Bovensmann, H., Buchwitz, M., Burrows, J. P., Deutscher, N. M., Griffith, D. W. T., Heymann, J., Macatangay, R., Messerschmidt, J., Notholt, J., Rettinger, M., Reuter, M., Sussmann, R., Velazco, V. A., Warneke, T., Wennberg, P. O., and Wunch, D.: Atmospheric greenhouse gases retrieved from SCIAMACHY: comparison to ground-based FTS measurements and model results, Atmos Chem Phys, 12, 1527-1540, DOI 10.5194/acp-12-1527-2012, 2012.

Schuck, T. J., Ishijima, K., Patra, P. K., Baker, A. K., Machida, T., Matsueda, H., Sawa, Y., Umezawa, T., Brenninkmeijer, C. A. M., and Lelieveld, J.: Distribution of methane in the tropical upper troposphere measured by CARIBIC and CONTRAIL aircraft, J Geophys Res-Atmos, 117, D19304, doi 10.1029/2012jd018199, 2012, in press.

Stutz, J., Oh, H. J., Whitlow, S. I., Anderson, C., Dibbb, J. E., Flynn, J. H., Rappengluck, B., and Lefer, B.: Simultaneous DOAS and mist-chamber IC measurements of HONO in Houston, TX, Atmospheric Environment, 44, 4090-4098, 10.1016/j.atmosenv.2009.02.003, 2010.

Thorpe, A. K., Roberts, D. A., Bradley, E. S., Funk, C. C., Dennison, P. E., and Leifer, I.: High resolution mapping of methane emissions from marine and terrestrial sources using a Cluster-Tuned Matched Filter technique and imaging spectrometry, Remote Sens Environ, 134, doi 10.1016/j.rse.2013.03.018, 2013.

Wennberg, P. O., Mui, W., Wunch, D., Kort, E. A., Blake, D. R., Atlas, E. L., Santoni, G. W., Wofsy, S. C., Diskin, G. S., Jeong, S., and Fischer, M. L.: On the Sources of Methane to the Los Angeles Atmosphere, Environ Sci Technol, 46, 9282-9289, doi 10.1021/Es301138y, 2012.

Woodwell, G. M., Mackenzie, F. T., Houghton, R. A., Apps, M., Gorham, E., and Davidson, E.: Biotic feedbacks in the warming of the earth, Climatic Change, 40, 495-518, 1998.

Wuebbles, D. J., and Hayhoe, K.: Atmospheric methane and global change, Earth-Sci Rev, 57, 177-210, doi 10.1016/S0012-8252(01)00062-9, 2002.

Wunch, D., Wennberg, P. O., Toon, G. C., Keppel-Aleks, G., and Yavin, Y. G.: Emissions of greenhouse gases from a North American megacity, Geophys Res Lett, 36, L15810, L15810 doi 10.1029/2009gl039825, 2009.

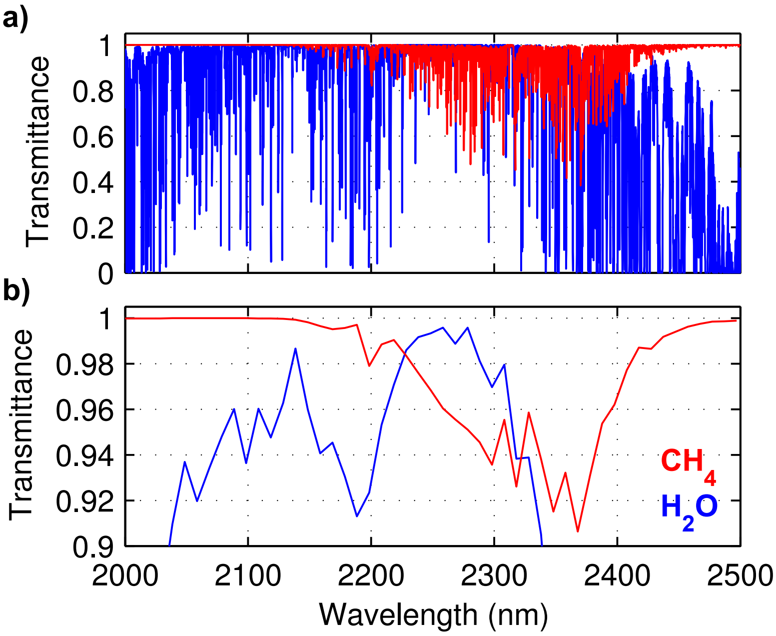

Figure 1. a. High resolution CH_4 and H_2O transmittance. b. Transmittance convolved to the 10 nm AVIRIS spectral resolution~~spectral sampling interval~~.

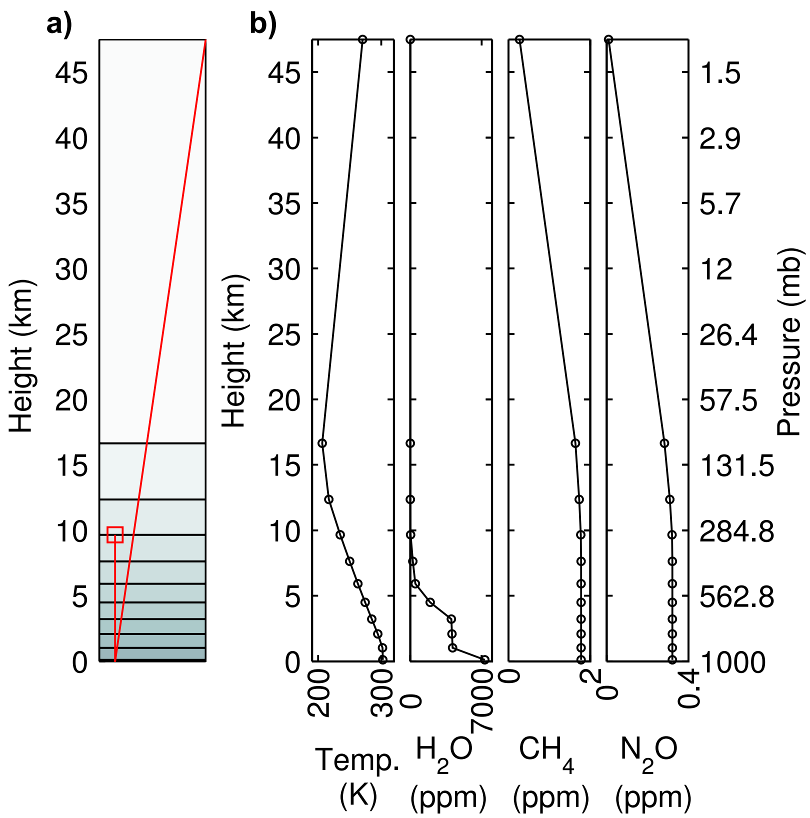

Figure 2. a. 10 atmospheric layers were used for retrievals (layer 1 at the top). For the COP scene, the aircraft was placed between layer 3 and 4 (red square). The slant and vertical light

paths (red lines) were used to scale optical densities appropriately. b. Profiles of temperature and VMR of H_2O, CH_4, and N_2O for the boundaries of each layer (black circles).

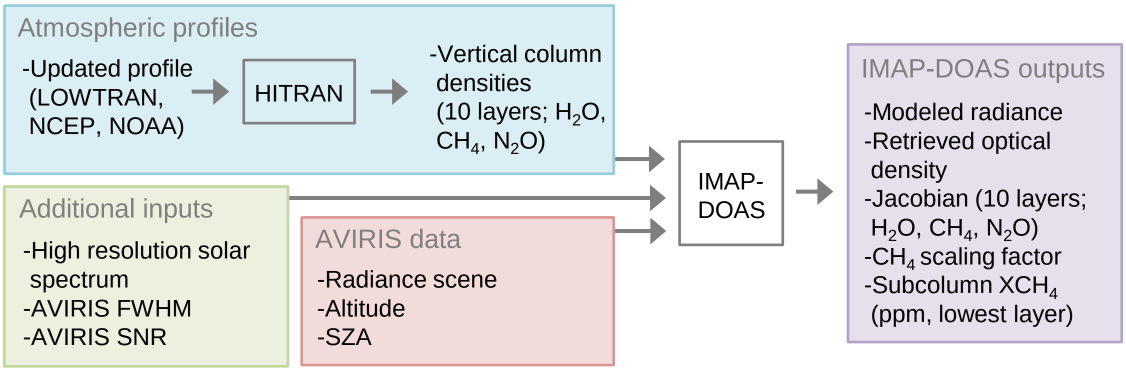

Figure 3. Processing steps for IMAP-DOAS CH_4 retrieval.

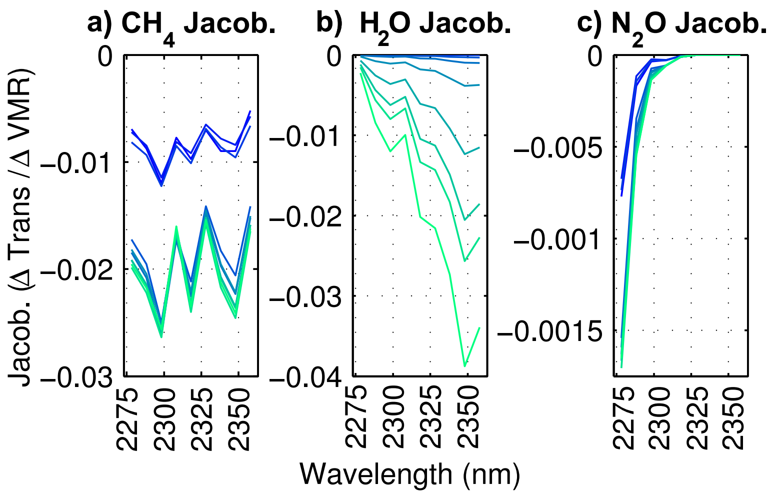

Figure 4. a. CH_4 Jacobian for each of the 10 atmospheric layers with colors transitioning from dark blue at the highest layer (layer 1) to light green for the lowest layer (layer 10). The CH_4 Jacobians with smaller magnitudes (dark blue) are for layers above the flight altitude. The same color scheme is used for the H_2O Jacobians (b) and N_2O Jacobians (c).

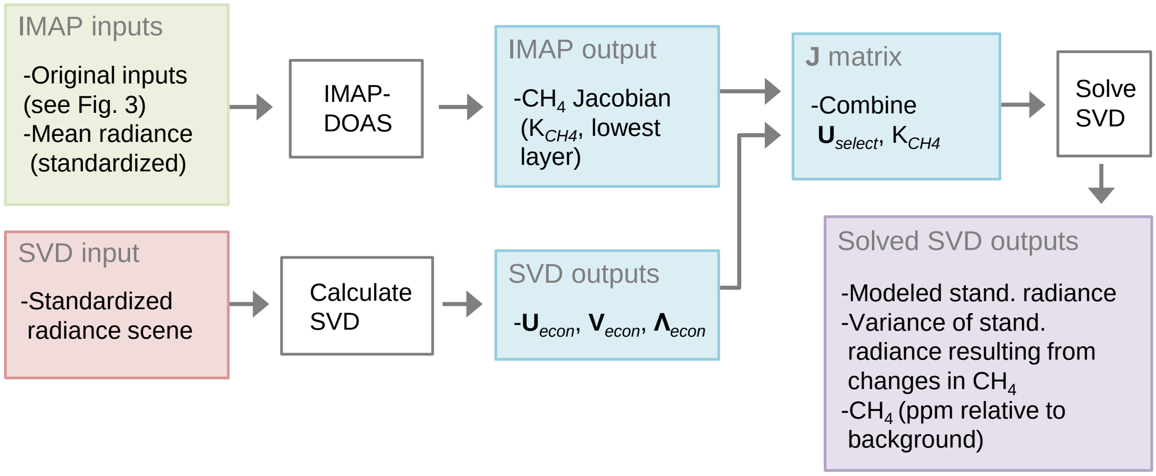

Figure 5. Processing steps for the SVD retrieval method. The IMAP-DOAS retrieval is performed on a mean radiance for the image subset to generate the CH_4 Jacobian for the lowest layer. The SVD is used to calculate $\mathbf{U}_{econ}$, $\mathbf{V}_{econ}$, and $\mathbf{\Lambda}_{econ}$ while $\mathbf{U}_{select}$ is combined with the CH_4 Jacobian to generate the **J** matrix. **J** is used to determine the portion of each radiance spectra associated with the CH_4 Jacobian (i.e. absorptions due to CH_4) and can be used to estimate CH_4 concentrations.

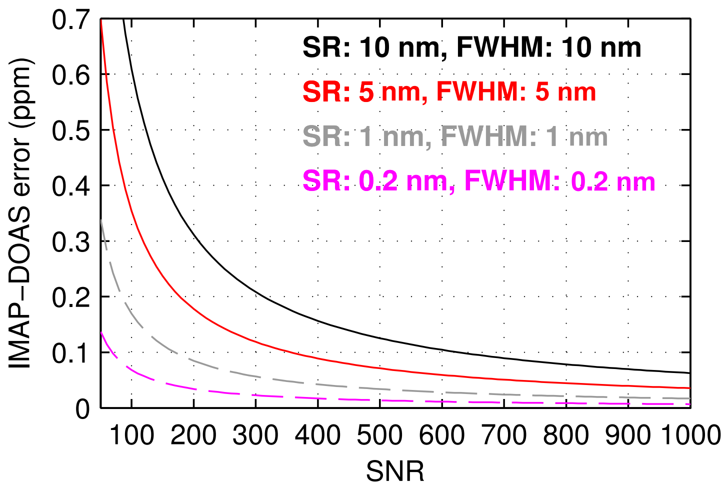

Figure 6. Estimated IMAP-DOAS retrieval errors (ppm CH_4) for four hypothetical sensors, each with the spectral resolution (SR)~~sampling interval (SSI)~~ equal to the FWHM. Errors are relative to lowest atmospheric layer (height up to 1.04 km) and decline with increased signal to noise ratio (SNR).

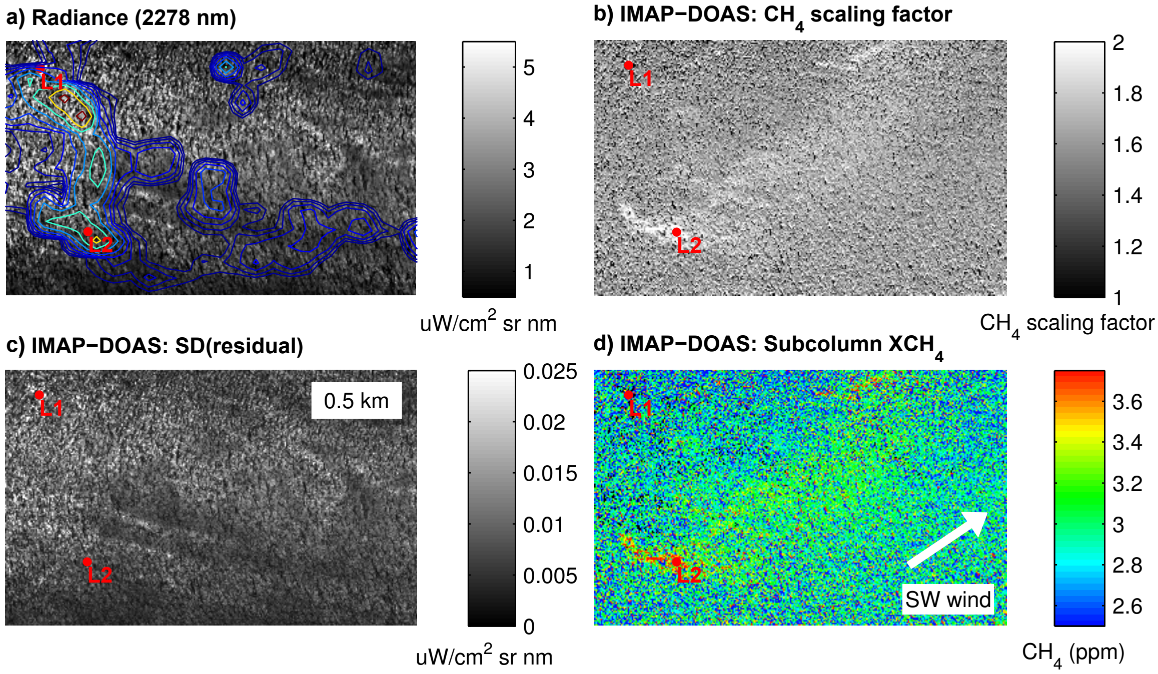

Figure 7. a. Measured radiance at 2,278 nm showing strong variability in brightness. Sonar return contours (Leifer et al., 2010) are overlain and correspond to known seep locations. b. For the same image subset, CH_4 scaling factor for the lowest atmospheric layer (layer 10) indicates a CH_4 plume consistent with the local wind direction. c. The standard deviation of the residuals (measured minus modeled radiance) depends strongly on brightness (a). d. Subcolumn XCH_4 (ppm CH_4 for the lowest layer) excluding bright pixels (greater than 5 $uWcm^{-2}sr^{-1}nm^{-1}$ in the fitting window) associated with high standard deviation of the residuals. For two spectra (indicated by location L1 and L2), measured and modeled radiance are provided in Fig. 8.

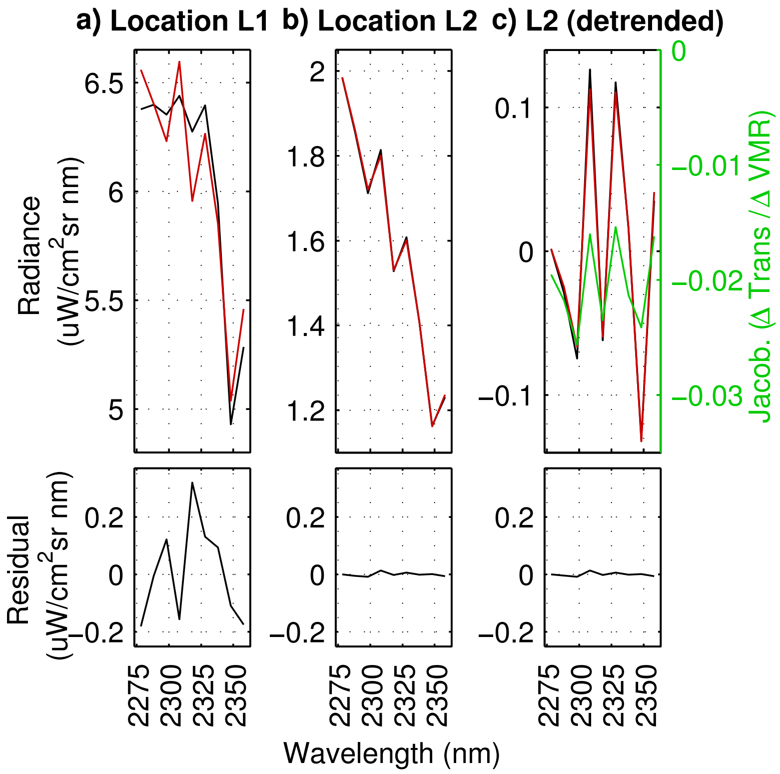

Figure 8. a. For location L1 (see Fig. 7), the measured radiance (black) indicates sensor saturation due to high sun-glint between 2,278 and 2,328 nm. This causes considerable disagreement with the modeled radiance (red), as indicated by the residual radiance shown in the bottom plot. b. There is better agreement for location L2. c. The radiance shown in b was detrended and the CH_4 Jacobian for the lowest layer overlain (green) to indicate the location of CH_4 absorptions at 2,298, 2,318, and 2,348 nm.

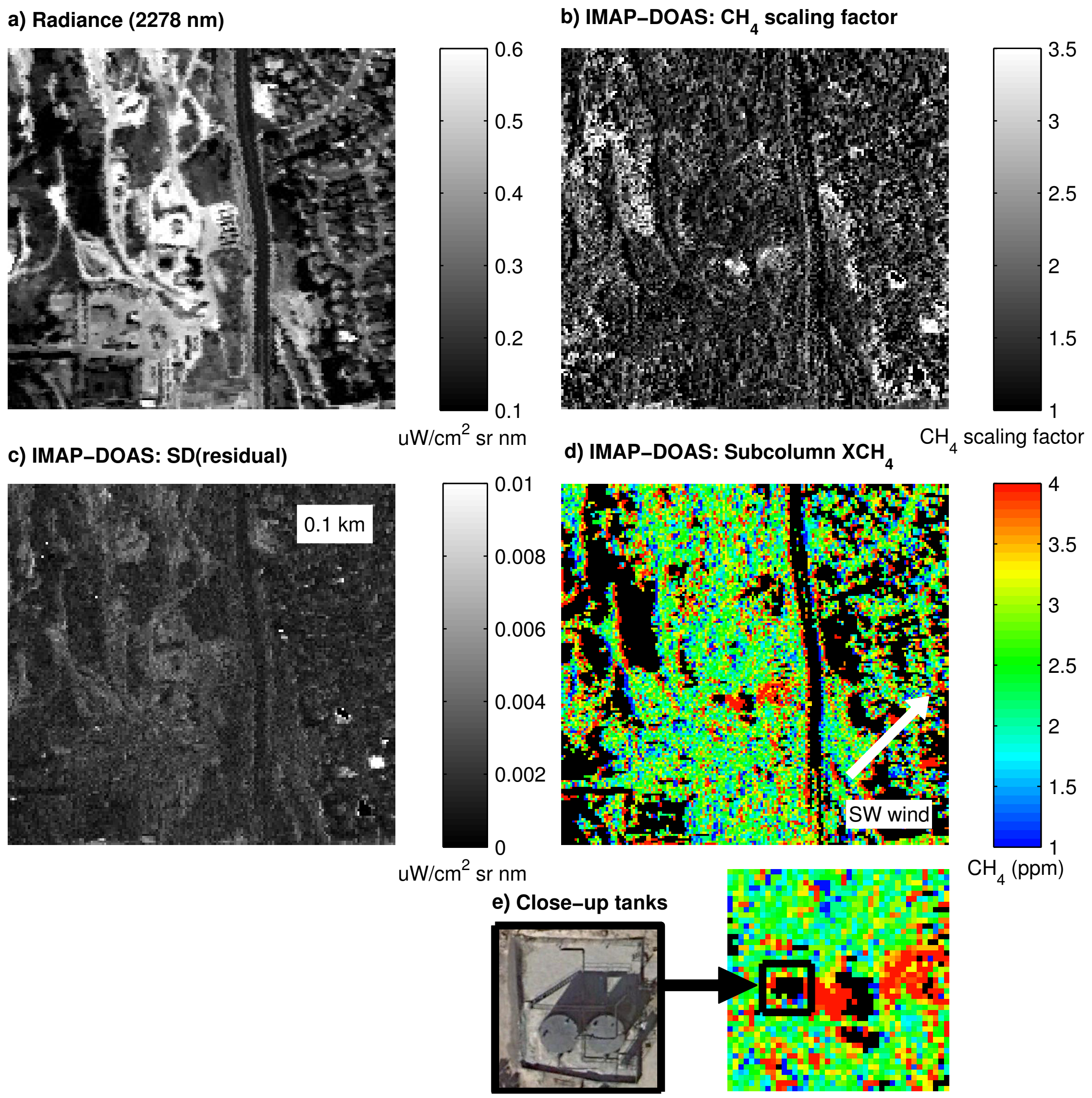

Figure 9. a. Radiance at 2,278 nm showing a portion of the Inglewood Oil Field. b. For the same image subset, CH_4 scaling factor for the lowest atmospheric layer (layer 10) appears heavily influenced by land surface type. c. Standard deviation of the residuals also appears influenced by land cover. d. Subcolumn XCH_4 (ppm CH_4 for the lowest layer) excluding dark pixels (less than 0.1 $uWcm^{-2}sr^{-1}nm^{-1}$ in the fitting window). e. Close-up of hydrocarbon storage tanks upwind of observed plume (Google Earth, 2013).

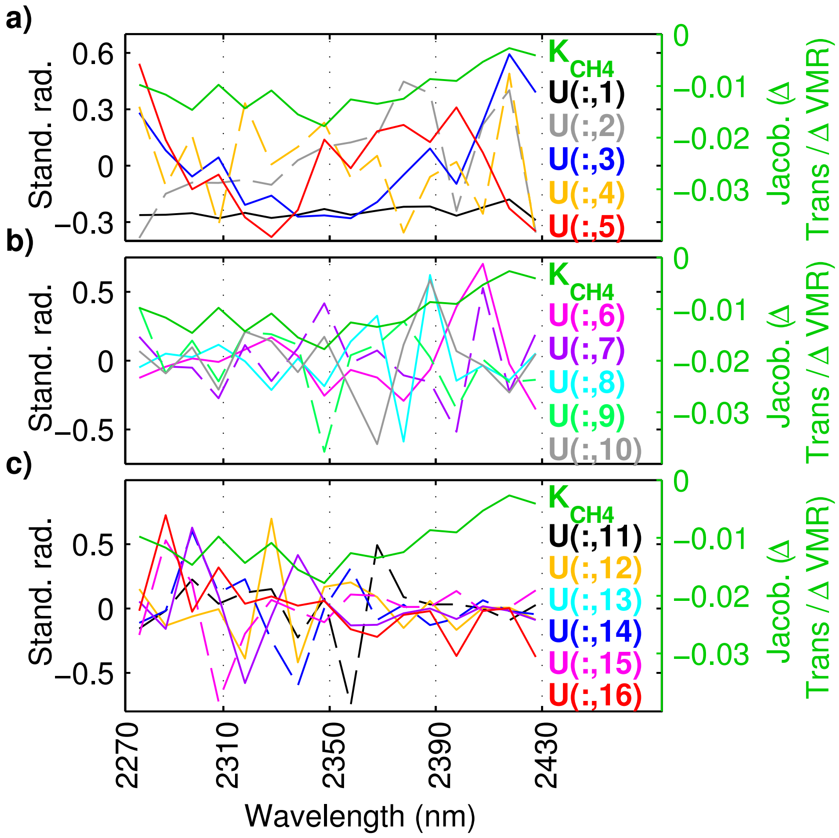

Figure 10. a. Singular vectors contained in $\mathbf{U}_{econ}$ for COP scene with CH_4 Jacobian ($\mathbf{K}_{CH4}$) plotted for reference.

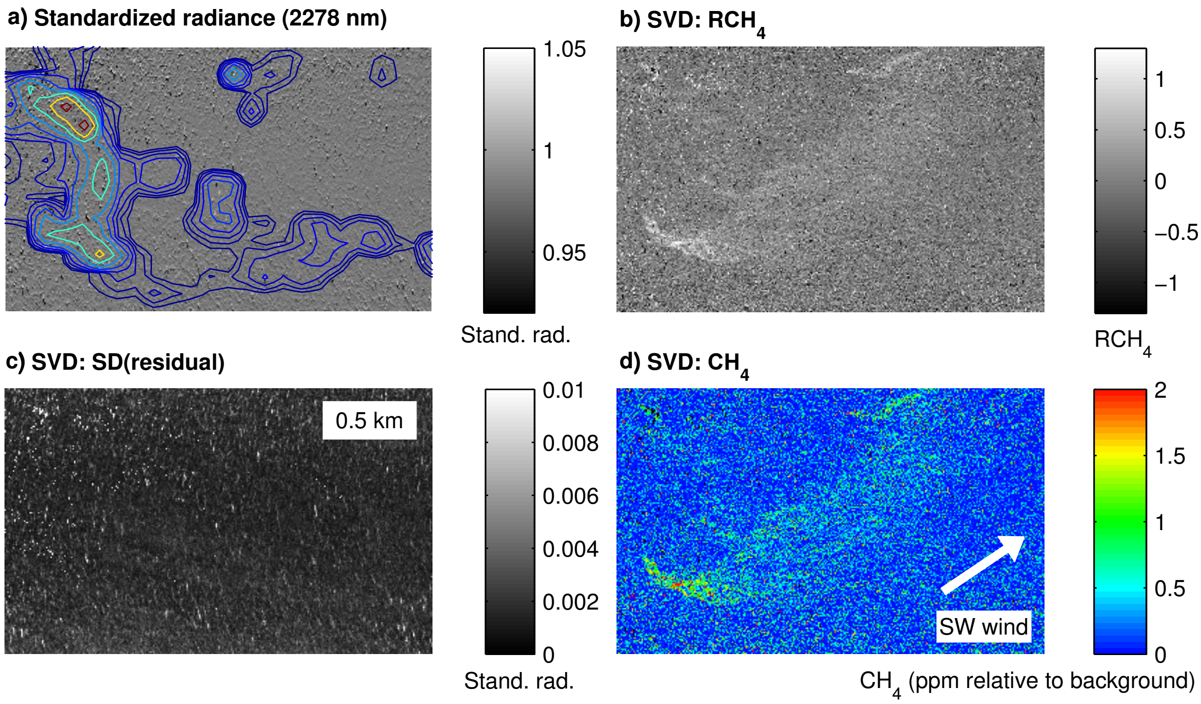

Figure 11. a. Standardized radiance used for calculating SVD at COP (showing only 2,278 nm). b. For the same image subset, RCH_4 results clearly indicate CH_4 plume. c. The standard deviation of the residuals (measured minus modeled radiance). d. ppm CH_4 relative to background excluding pixels with greater than 0.0075 standard deviation of the residual (a unitless value given the SVD was performed on standardized radiance).

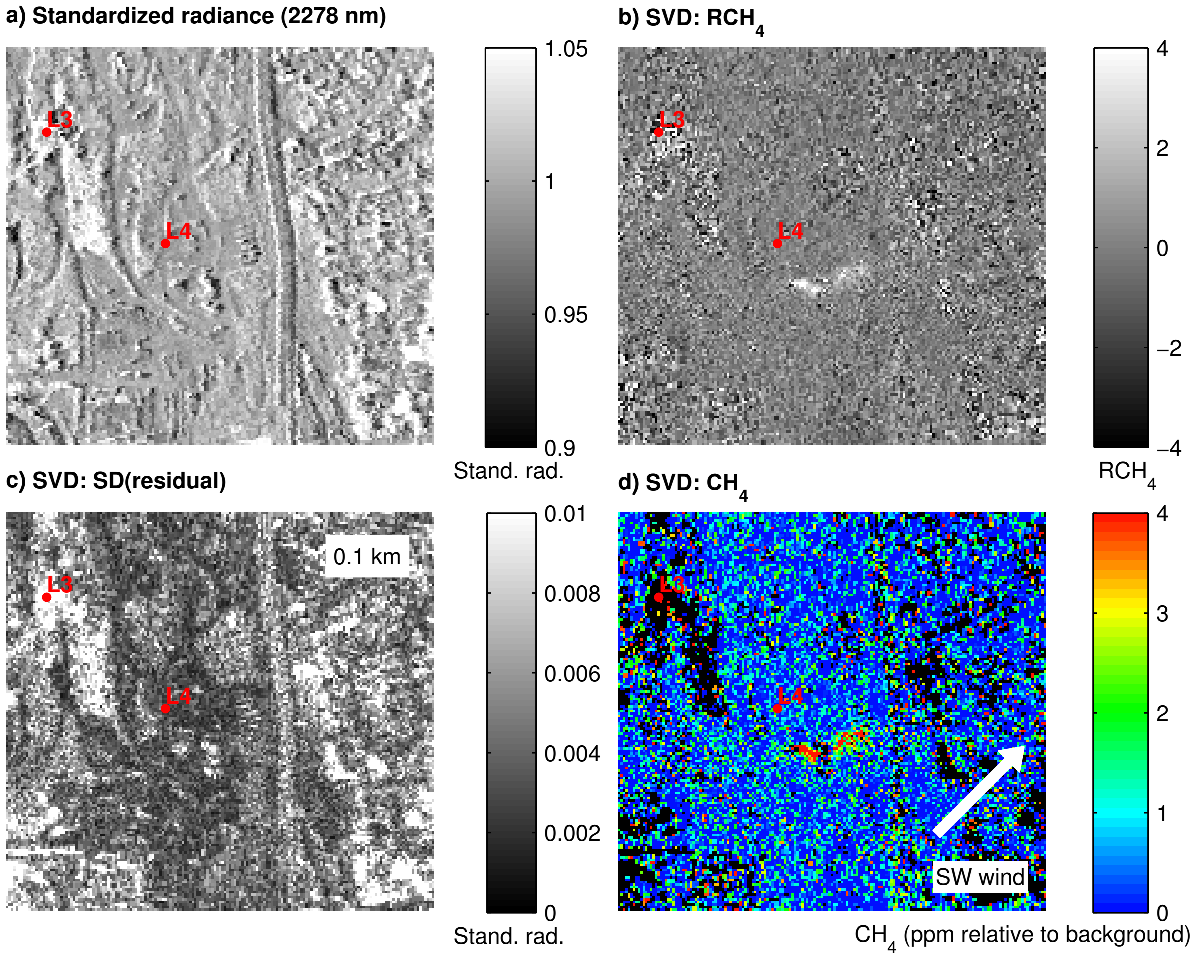

Figure 12. a. Standardized radiance used for calculating SVD for Inglewood subset (showing only 2,278 nm). b. For the same image subset, RCH_4 results indicate CH_4 plume at the center of the scene. c. The standard deviation of the residuals (measured minus modeled radiance). d. ppm CH_4 relative to background excluding pixels with greater than 0.0075 standard deviation of the residual (a unitless value given the SVD was performed on standardized radiance). For two spectra (indicated by location L3 and L4), measured and modeled radiance are provided in Fig. 13.

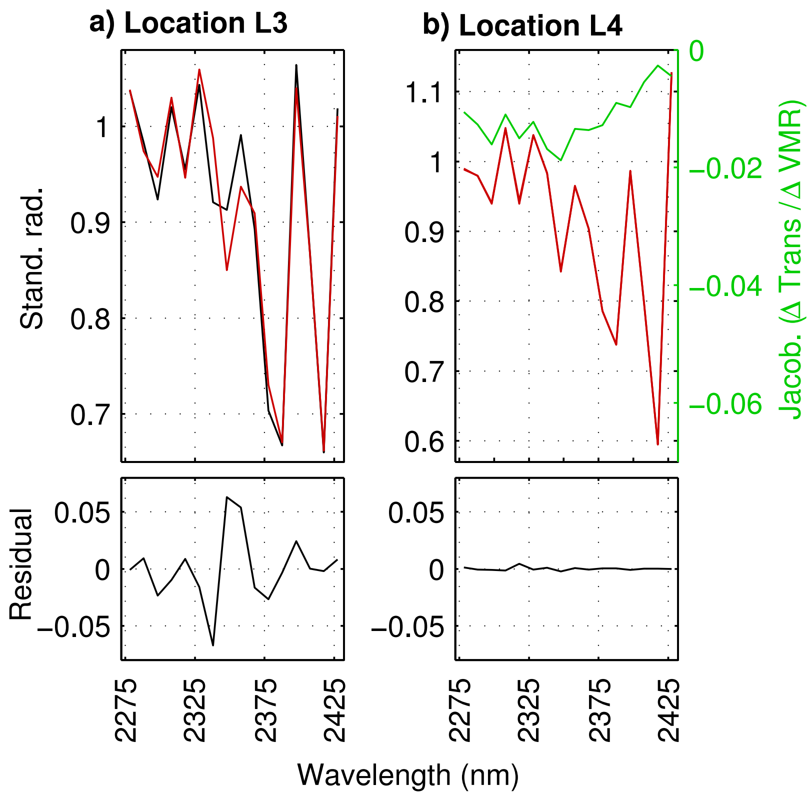

Figure 13. a. The modeled (red) and measured standardized radiance (black) for location L3, which corresponds to a dark spectrum with an average radiance of 0.0376 uWcm^{-2}sr^{-1}nm^{-1}. L3 is located in a distinct region with high values for the standard deviation of the residuals (see Fig. 12c) and was excluded from the results shown in Fig. 12d. b. For location L4, there is better agreement between modeled and measured radiance (average 0.5187 uWcm^{-2}sr^{-1}nm^{-1}). The CH_4 Jacobian for the lowest layer is overlain (green) to indicate the location of CH_4 absorptions.

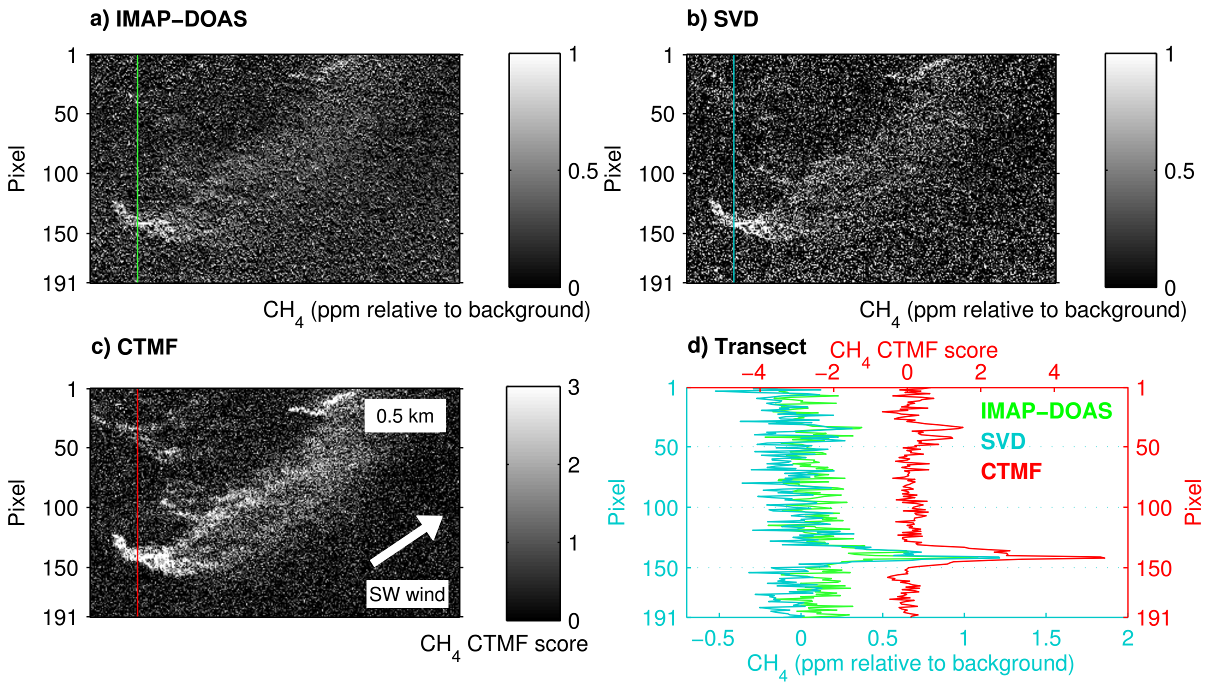

Figure 14. For the same COP subset, there is good agreement between results obtained using three techniques. a. IMAP-DOAS. b. SVD. c. Cluster-Tuned Matched Filter (CTMF). The location of a vertical transect is shown for the IMAP-DOAS (green line), SVD (cyan), and CTFM results (red). d. Values along the transect are shown for IMAP-DOAS (green), SVD (cyan), and CTMF (red). At each point along the transect, an average value was calculated for 21 pixels centered on the transect in the horizontal direction. IMAP-DOAS and SVD transects share the cyan figure axes, while the CTMF transect was offset for clarity and corresponds to the red figure axes.

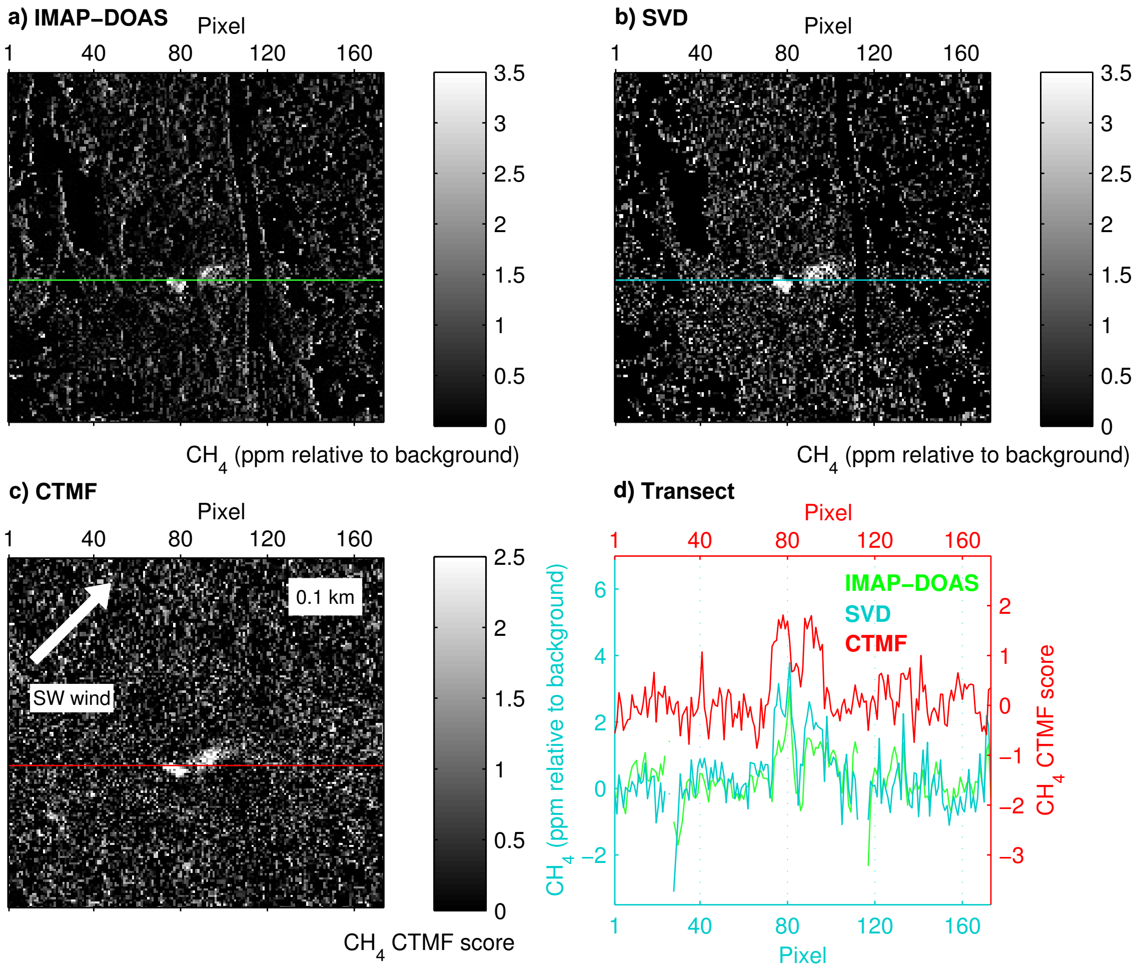

Figure 15. For the same Inglewood subset, there is good agreement between results obtained using three techniques. a. IMAP-DOAS. b. SVD. c. Cluster-Tuned Matched Filter (CTMF). The location of a horizontal transect is shown for the IMAP-DOAS (green line), SVD (cyan), and CTMF results (red). d. Values along the transect are shown for IMAP-DOAS (green), SVD (cyan), and CTMF (red) approach. At each point along the transect, an average value was calculated for 9 pixels centered on the transect in the vertical direction. IMAP-DOAS and SVD transects share the cyan figure axes, while the CTMF transect was offset for clarity and corresponds to the red figure axes.

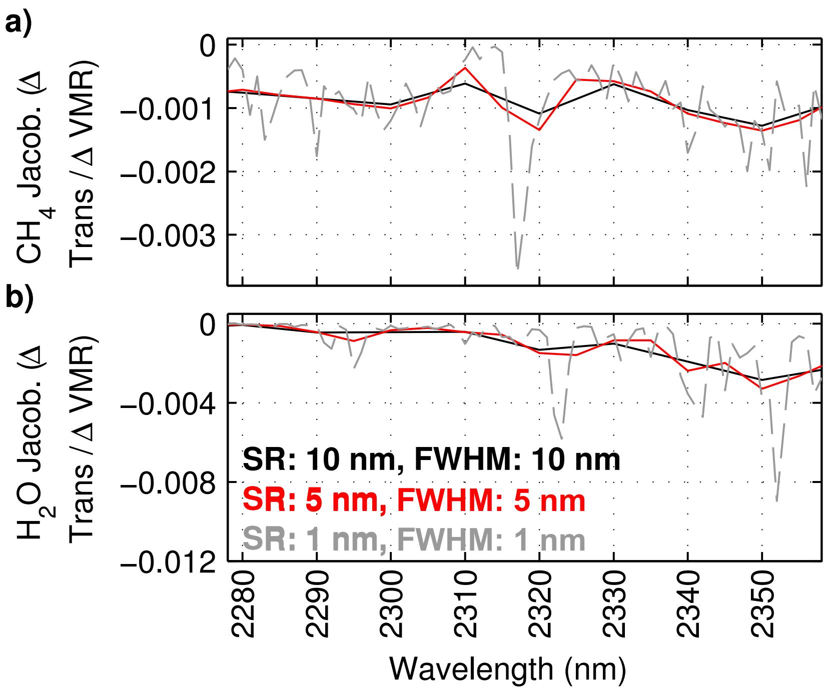

Figure 16. a. For the lowest layer of the atmopsheric model (height up to 1.04 km), the CH_4 Jacobian calculated for AVIRISng (red) indicates improved sensitivity compared to the CH_4 Jacobian for AVIRIS (black). Even greater sensitivity can be achieved using a finer spectral resolution (SR)~~SSI~~ and FWHM (dashed grey). b. H_2O Jacobians calculated for the same three sensors.